Pseudogap and Anderson localization of light in correlated disordered media

R. Monsarrat ⬛,[*] R. Pierrat ⬛, A. Tourin, and A. Goetschy[†]
Institut Langevin, ESPCI Paris, PSL University, CNRS, 75005 Paris, France

Among the remarkable scattering properties of correlated disordered materials, the origin of pseudogaps and the formation of localized states are some of the most puzzling features. Fundamental differences between scalar and vector waves in both these aspects make their comprehension even more problematic. Here we present an in-depth and comprehensive analysis of the order-to-disorder transition in 2D resonant systems. We show with exact *ab initio* numerical simulations in finite-size hyperuniform media that localization of 2D vector waves can occur in the presence of correlated disorder, in a regime of moderate density of scatterers. On the contrary, no signature of localization is found for white noise disorder. This is in striking contrast with scalar waves, which localize at high density whatever the amount of correlation. For correlated materials, localization is associated with the formation of pseudogap in the density of states. We develop two complementary models to explain these observations. The first one uses an effective photonic crystal-type framework and the second relies on a diagrammatic treatment of the multiple scattering sequences. We provide explicit theoretical evaluations of the density of states and localization length in good agreement with numerical simulations. In this way, we identify the microscopic processes at the origin of pseudogap formation and clarify the role of the density of states for wave localization in resonant correlated media. The generality of our framework makes possible to apply our predictions for a large variety of scattering systems including dielectric structures with high quality factor, cold atoms, artificial atoms, as well as microwave resonators.

I. INTRODUCTION

Light scattering in heterogeneous media is deeply affected by the existence of spatial correlations in the material structure [1,2]. Transparency of the cornea [3], structural blue color of bird feathers [4], or strong anisotropic scattering in dense colloidal liquids [5] are representative examples of the impact of correlated disorder (CD) on optical properties. Remarkably, these effects can be understood in a simple manner from the dependence of the transport mean free path of light ℓ_t on the pair correlation function h_2 of the medium. For monochromatic light of wavenumber $k = 2\pi/\lambda$ propagating in a disordered medium with number density ρ, the inverse transport mean free path is $\ell_t^{-1} \sim \rho \int_0^{2k} dq F(q) S(q)$, where $S(q) = 1 + \rho h_2(q)$ is the structure factor and $F(q)$ a function proportional to the form factor of individual scatterers [2,6]. The interplay between local Mie resonance and nonlocal spatial correlations fully determines the transmission and reflection spectra of the material: $T(\lambda) \sim \ell_t/L$ and $R(\lambda) = 1 - T(\lambda)$ for a nonabsorbing medium of thickness $L > \ell_t$.

On the other hand, other fundamental properties of CD materials still withstand simple explanation. This is the case of bandgaps or pseudogaps found in the photonic density of states (DOS). Although pseudogaps are naturally expected in photonic crystals with imperfections (as a result of partial gap filling by defect states) [7,8], their presence in 2D and 3D materials without any periodicity remains puzzling [9–11]. Contrary to the mean free path, there is no available theory predicting photonic bandgaps (PBGs) in these systems [1,2,12]. There is also no clear consensus on the physical mechanisms at their origin. The role of stealth hyperuniformity was put forward in Ref. [13], but a recent numerical study showed that short-range order was actually sufficient to observe similar PBG [14]. The absence of a periodic lattice or long-range order makes the Bragg interference scenario unreliable. It is thus tempting to describe PBG in CD materials as the result of coupling between local resonances (such as Mie resonances). The key role of local resonances in PBG formation has already been emphasized for photonic crystals and photonic networks [15–18], as well as for dense media made of subwavelength resonators where propagation is essentially ballistic and exhibits a polaritonic dispersion relation [19]. In this context, a description based on nearest-neighbor tight-binding coupling between resonances—similar to the one used for the computation of the electronic DOS of amorphous semiconductors [20,21]—is appealing. However, as we will demonstrate, this approach fails to capture polaritonic gaps. One objective of the present paper is to provide a theoretical and comprehensive analysis for disordered media where multiple scattering plays a prominent role.

[*]romain.monsarrat@espci.psl.eu
[†]arthur.goetschy@espci.psl.eu

A second remarkable feature of CD materials is their ability to induce Anderson localization of light. In recent years, localized states have been found numerically and experimentally in various amorphous correlated structures without remanent periodicity [22–25]. In addition, both pseudogap and localization of scalar waves have been observed in 2D hyperuniform materials, although no explanation has been provided for their concomitance [12,26]. In a first approach, localization can be thought to be related to the strong modulation of ℓ_t mentioned above. Indeed, for scalar waves, reducing ℓ_t by a proper choice of the form and structure factors is expected to favor wave localization both in 3D and 2D. A genuine localization transition is thought to occur in 3D for $k\ell_t \sim 1$, whereas in 2D, the commonly used expression of the localization length, $\xi \sim \ell_t e^{\pi k \ell_t / 2}$, quickly becomes larger than the system size and physically irrelevant in realistic samples for $k\ell_t \gg 1$; only infinite 2D systems exhibit localization for arbitrary $k\ell_t$ [27]. Such control of the localization length has been investigated numerically in Ref. [24]. However, the use of previous 2D formula in CD materials presenting potentially strong local resonances is questionable for two reasons. First, it ignores the strong modification of the energy velocity and diffusion coefficient of light in resonant materials [19]. Second, it fails to reveal the role of the DOS for localization, whereas localized states have been observed in the bands near the gap edge [12,23,26,28]. John was the first to highlight in a seminal work the crucial role of the DOS depletion for photon localization and the necessity to modify the standard Ioffe-Regel criterion established initially for unperturbed DOS of free waves [7,29,30]. His initial rigorous treatment considered slightly disordered photonic crystals [7], where localization occurs in the vicinity of the original Bragg gap, and is, as such, inapplicable for CD materials where local resonances are prominent and periodicity absent. As we will demonstrate, both the origin of the gap and the shape of the DOS in its vicinity differ from those considered in John's model. However, the general frameworks of the scaling theory [30,31] and self-consistent theory of localization [32], which explicitly involve the DOS, still apply, allowing to make an explicit connection between localization and DOS depletion. This connection has been somewhat not sufficiently appreciated in the study of disordered photonic structures and it is another objective of this paper to highlight it.

In this study, we propose a thorough analysis of the photonic DOS and localization signatures in 2D CD materials made of resonant dipole scatterers. These materials allow an accurate representation of light scattering by atoms or local inhomogeneities supporting well-defined Mie-type resonances. They have been used in recent studies of DOS and localization for both photonic crystals [33–35] and fully disordered materials [36–40]. Here we probe the continuous transition from full disorder to complete order by tuning the degree of stealth hyperunifomity of the dipole pattern. Importantly, our analysis emphasizes the differences between out-of plane and in-plane dipole excitations, respectively due to transverse magnetic (TM) and transverse electric (TE) field propagation. In the first case, the field exciting the dipoles is perpendicular to the 2D plane, so that the scatterers behave as effective in-plane monopoles and wave propagation reduces to a regular scalar problem. In the second case, the exciting field

lies in the 2D plane, where the dipoles can have different orientations: We refer to this situation as a vectorial light scattering problem. Recently, it has been demonstrated that the longitudinal coupling in 3D between fully disordered point scatterers indirectly opens a new propagation channel at high density that prevents Anderson localization to occur [37,41–43]. For in plane propagation in 2D disordered point dipole systems, this longitudinal coupling is also present and as a result, no evidence of localized states has been reported so far [39]. These recent observations have boosted the search for vector wave localization in amorphous photonic materials with spatial correlations [2,25].

In Sec. II, we report the observation of localized states for TE (vector) waves in CD dipole point patterns of finite size, that are clearly absent without spatial correlations. To our knowledge, such observation has not been reported before. Remarkably, TE localization occurs at moderate density and disappears at high density, whereas TM (scalar) waves are localized at high density only. In addition, we show that localization is concomitant to the formation of pseudogaps in the DOS. To elucidate these observations, we develop two complementary approaches, presented in Sec. III and Sec. IV, respectively. The first one uses an effective photonic crystal-type framework that expounds gap formation as the result of the superposition of different polaritonic dispersion relations inside the effective Brillouin zone. This approach applies both for TE and TM waves and predicts accurately the critical densities for which pseudogap appear and disappear. In Sec. IV, we establish a general expression of the DOS for an assembly of high-Q resonators, that turns out to be different from the commonly accepted expression of the DOS. We then compute it theoretically for TE waves at moderate density using a diagrammatic expansion including both spatial correlation and recurrent scattering. Good agreement is found with direct numerical simulation of the DOS. This approach allows us to identify microscopic scattering processes at the origin of the DOS depletion. Finally, in Sec. V, we express the equations of the self-consistent theory of localization in 2D in terms of the DOS to reveal how the localization length ξ explicitly depends on it. This prediction turns out to be in good agreement with direct evaluation of ξ from simulation. Hence, this paper clarifies both the origin of pseudogap and localization of vector waves in 2D correlated and locally resonant materials.

II. DENSITY OF STATES AND LOCALIZATION OF 2D VECTOR WAVES

A. Resonances in finite-size hyperuniform materials

In this study, we consider light propagation at frequency $\omega = ck$ in an ensemble of N identical resonant scatterers characterized by their polarizability $\alpha(\omega)$. The field $\mathbf{E}_i$ exciting a scatterer i is the sum of the input external field $\mathbf{E}_0(\mathbf{r}_i)$ and the fields radiated by scatterers $j \neq i$,

$$\mathbf{E}_i = \mathbf{E}_0(\mathbf{r}_i) - k^2 \alpha(\omega) \sum_{j \neq i} \mathbf{G}_0(\mathbf{r}_i, \mathbf{r}_j, \omega) \mathbf{E}_j. \quad (1)$$

Here, $\mathbf{G}_0$ is the free space Green's function of the wave equation, propagating the field between different scatterers. In 2D systems (invariant along direction z), $\mathbf{G}_0$ is a scalar for TM

polarization and a 2×2 matrix for TE polarization. Explicit expressions of $\mathbf{G}_0$ are given in Appendix A. The derivation of coupled equations (1), in a semiclassical [44,45] or full quantum framework [46,47], shows that $\alpha(\omega)$ also depends on the field polarization. Once the self-consistent system (1) is solved, the field at any position $\mathbf{r}$ is $\mathbf{E}(\mathbf{r}) = \mathbf{E}_0(\mathbf{r}) - k^2\alpha(\omega)\sum_i \mathbf{G}_0(\mathbf{r}, \mathbf{r}_i, \omega)\mathbf{E}_i$. As a prototype system represented by such equations, we can think of subwavelength resonant and long cylinders aligned along the z direction. These equations can represent more elaborate structures as well, such as thin metallic waveguides filled with small high dielectric cylinders [26]. In the latter case, the "TM/TE polarization" terminology should be replaced by the more general "out-of-plane/in-plane dipole resonance" terminology, as the dipolar excitations can be either electric or magnetic for a given polarization.

By definition, resonances of this scattering problem are solutions ω in the absence of external excitation ($\mathbf{E}_0 = \mathbf{0}$). According to Eq. (1) they satisfy the equation

$$\det[\mathbb{1} + k^2\alpha(\omega)\mathbb{G}_0(\omega)] = 0, \qquad (2)$$

where $\mathbb{G}_0(\omega)$ is a $\beta N \times \beta N$ matrix ($\beta = 1$ for scalar waves and $\beta = 2$ for vector waves) with ij element ($i \neq j$) equal to $\mathbf{G}_0(\mathbf{r}_i, \mathbf{r}_j, \omega)$ and ii element equal to $\mathbf{0}$. Equation (2) rigorously captures all the poles of the scattering operator, except those associated to peculiar field solutions that are zero on each scatterer ($\mathbf{E}_i = 0$ for all i). The latter, which behave as free field without matter, may exist in crystals because of the periodicity [48,49] but are unlikely for disordered materials. In the following, the polarizability of each scatterer is assumed to have a single resonance at ω_0 and a radiative decay rate Γ_0. For $|\omega - \omega_0| \ll \omega_0$, it takes the form $\alpha(\omega) = 4\beta\tilde{\alpha}(\omega)/k_0^2$, with $k_0 = \omega_0/c$ and

$$\tilde{\alpha}(\omega) = \frac{-\Gamma_0/2}{\omega - \omega_0 + i\Gamma_0/2}. \qquad (3)$$

The resonance condition (2) is then conveniently expressed in terms of an effective Hamiltonian $\mathcal{H}(\omega)$ as $\det[\omega\mathbb{1} - \mathcal{H}(\omega)] = 0$, with

$$\mathcal{H}(\omega) = \left(\omega_0 - i\frac{\Gamma_0}{2}\right)\mathbb{1} - \frac{\Gamma_0}{2}\tilde{\mathbb{G}}_0(\omega), \qquad (4)$$

and $\tilde{\mathbb{G}}_0(\omega) = -4\beta(\omega/\omega_0)^2\mathbb{G}_0(\omega)$. In this way, light-matter interaction is entirely characterized by an effective potential proportional to the Green's matrix $\tilde{\mathbb{G}}_0(\omega)$ [33,47,50]. For $N \gg 1$ scatterers, the frequency dependance of $\tilde{\mathbb{G}}_0(\omega)$ makes the search of resonances a cumbersome nonlinear problem, which can be treated exactly for periodic point patterns (see discussion in Sec. III), but not for the broad class of hyperuniform patterns considered in this paper. In the following, we will address the case of scattering resonators with large quality factor ($Q = \omega_0/\Gamma_0 \gg 1$), for which the coupling term in Eq. (4) can be treated as a perturbation. This amounts to freeze the frequency of $\tilde{\mathbb{G}}_0(\omega)$ at the resonance frequency ω_0. This is an excellent approximation for light scattering in atomic systems, which we expect to hold as well for Mie-type resonators with $Q \gtrsim 10$. In this situation, there are βN complex resonances $\omega_n - i\Gamma_n/2$ given by

$$\begin{cases} \omega_n = \omega_0 - \dfrac{\Gamma_0}{2}\mathrm{Re}\Lambda_n, \\[2mm] \Gamma_n = \Gamma_0(1 + \mathrm{Im}\Lambda_n), \end{cases} \qquad (5)$$

where Λ_n are the eigenvalues of the Green's matrix $\tilde{\mathbb{G}}_0(\omega_0)$. For finite-size system, Λ_n occupy an extended domain in the complex plane, with $\mathrm{Im}\Lambda_n > -1$ [51]. $\mathrm{Re}\Lambda_n$ represent collective Lamb shifts and $\mathrm{Im}\Lambda_n$ collective decay rates. The distribution of Λ_n in the complex plane has been characterized theoretically in details for scalar and vector waves in 3D fully disordered systems [36,47,51,52]. In particular, finite mode life-times due to finite system size offer valuable information about localization properties of the corresponding eigenstates [36–38,40].

To probe the impact of the disorder-to-order transition on the resonances of the system, we arranged the 2D scatterers inside a disk of radius R using stealthy hyperuniform (SHU) point patterns [53,54]. The latter are configurations $\{\mathbf{r}_i\}$, which minimize to zero the structure factor $S(\mathbf{q}) = 1 + \rho h_2(\mathbf{q})$ in a domain $|\mathbf{q}| < K$. In practice, they are found by minimizing the two-body potential [14,55]

$$U(\{\mathbf{r}_i\}) = \int_{q<K} d\mathbf{q}\,\tilde{S}(\mathbf{q}) \equiv \sum_{i,j} u(\mathbf{r}_i - \mathbf{r}_j), \qquad (6)$$
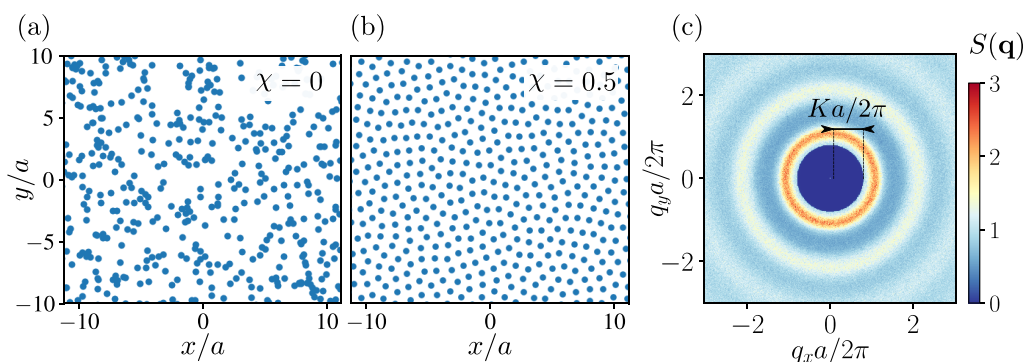

FIG. 1. [(a),(b)] Typical arrangements of scatterers corresponding to different degrees of spatial correlation. The continuous transition from white noise disorder (a), to strongly correlated material (b), and eventually to crystal, is probed by tuning the degree of stealth hyperuniformity $0 \leqslant \chi \lesssim 0.8$. (c) Isotropic structure factor of the correlated pattern shown in (b), which exhibits a dominant peak in $q \simeq 2\pi/a$ ($a = \rho^{-1/2}$ is the mean distance between scatterers). The procedure used to generate the pattern imposes $S(\mathbf{q}) = 0$ for $q < K$ (see text for details).
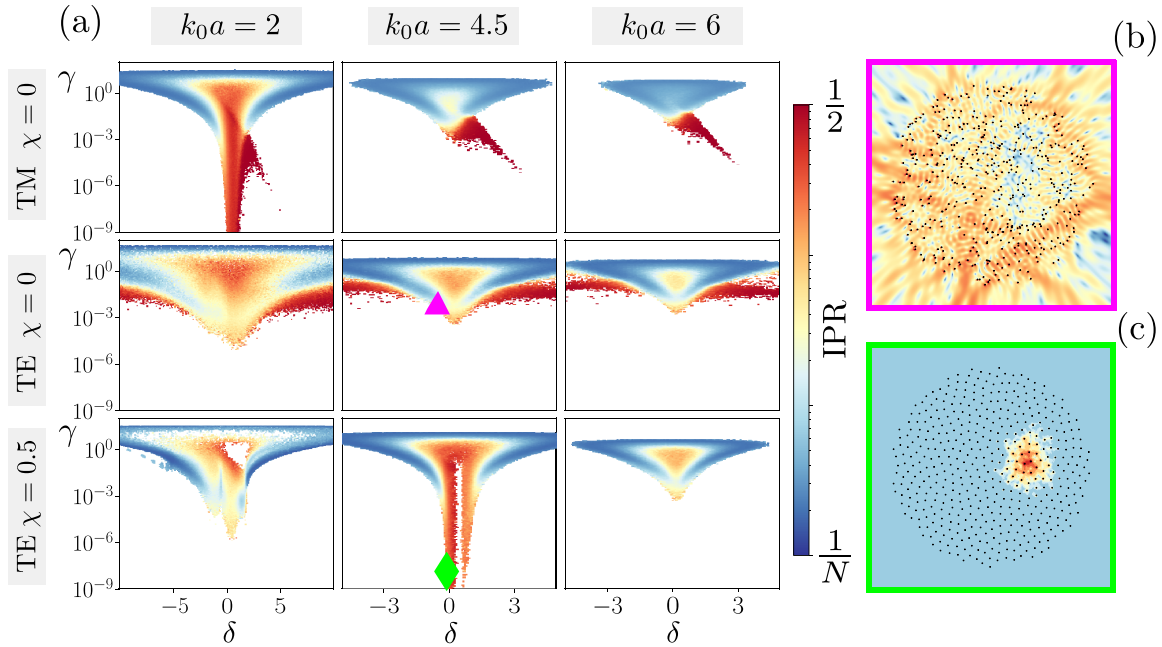
FIG. 2. (a) Distribution of resonances $\omega_n - i\Gamma_n/2$ in the complex plane for different densities (columns) and degree of correlation or polarization (rows). Axes are labeled with normalized units [$\delta = 2(\omega - \omega_0)/\Gamma_0$ stands for detuning and $\gamma = \Gamma/\Gamma_0$ for decay rate]. The color refers to the inverse participation ratio of the corresponding eigenvectors in log scale. The system size is $k_0 R = 55$ and the number of disorder realizations adjusted to have a number of eigenvalues of the order of 10^6. [(b),(c)] Typical spatial profiles in log scale of the intensity generated by exciting selectively eigenvectors associated to the eigenvalues marked with triangle (b) and diamond (c) in the complex plane.

where $\tilde{S}(\mathbf{q}) = \sum_{i,j} e^{i\mathbf{q}\cdot(\mathbf{r}_i-\mathbf{r}_j)}/N$, and $u(\Delta\mathbf{r}) = 2\pi K$ $J_1(K\Delta r)/\Delta r$ in the limit $R \to \infty$. We refer to Appendix B for more details about the pattern generation and the explicit link between $S(\mathbf{q})$ and $\tilde{S}(\mathbf{q})$. The amount of spatial correlation is controlled by the stealthiness parameter χ defined as the ratio between the number of constrained degrees of freedom in reciprocal space ($NK^2a^2/8\pi$) and the total number of spatial degrees of freedoms ($2N$),

$$\chi = \frac{(Ka)^2}{16\pi}, \qquad (7)$$

where $a = \rho^{-1/2} = \sqrt{\pi/N}R$ is the mean distance between scatterers. When χ is progressively increased from 0, the structure factor goes from a flat response $S(\mathbf{q}) = 1$ for white noise disorder [see Fig. 1(a) for a typical configuration] to a peaked profile that remains isotropic as long as $\chi \lesssim 0.6$. Crystalline order is achieved for $\chi \simeq 0.7 - 0.8$ when K coincides with the first Bragg peak of the crystalline lattice. As an illustration, we show a typical disorder configuration for $\chi = 0.5$ in Fig. 1(b) and the corresponding isotropic structure factor in Fig. 1(c). Such isotropic profile of $S(\mathbf{q})$, with a first dominant peak at $q \simeq 2\pi/a$, is very similar to the profile obtained with hard disks at sufficiently large packing fraction [14]. Since all our predictions for pseudogap and localization established in the following are expressed in terms of $h_2(\mathbf{r})$ or $S(\mathbf{q})$, we expect them not to be specific to SHU patterns, but rather generic for any type of correlated systems with similar structure factor.

B. Distribution of resonances in the complex plane and IPR

The effect of correlated disorder on scattering can be apprehended by visualizing the repartition of resonances $\omega_n - i\Gamma_n/2$ in the complex plane, as shown in Fig. 2(a). For convenience, frequencies and decay rates are expressed with normalized units, $\delta_n = 2(\omega_n - \omega_0)/\Gamma_0$ and $\gamma_n = \Gamma_n/\Gamma_0$. The degree of localization of the corresponding eigenstates ψ_n (of components $\psi_{n,i}$ at positions $\mathbf{r}_i$) is also shown, using the inverse participation ratio $\text{IPR}_n = \sum_i^N \|\psi_{n,i}\|^4/(\sum_i^N \|\psi_{n,i}\|^2)^2$ as color scale. We first analyze the IPR map of scalar waves without correlation (first line), which will serve as reference for the understanding of vector waves (second and third lines). At low density ($k_0a = 6$), resonances spread around the central frequency ω_0 with decay rates covering the range $\gamma \in [10^{-3}, 10]$, while most states are delocalized (low IPR). The smallest decay rates stand for proximity resonances formed at $\delta > 0$. They are due to localized states on pairs of close scatterers ($\text{IPR}_n \sim 1/2$) and are unrelated to Anderson localization [36,37,52]. On the other hand, at large density ($k_0a = 2$), a long tail of resonances with very small decay rates ($\gamma \in [10^{-15}, 10^{-6}]$) is clearly visible near $\delta = 0$. It is associated to states with large IPR localized in the bulk of the scattering medium. These signatures mark the onset of Anderson localization, as already studied for scalar waves both in 3D [37,38,40] and 2D [39]. Here localization is triggered by a reduction of the transport mean free path ℓ_t at large density and small detuning [19]. Approaches to localization in 3D and 2D are expected to be different since a genuine transition occurs in 3D at $k_0a \simeq 2.3$ corresponding to $k_0\ell_t \sim 1$ [56],

whereas in 2D, the critical density below which localization is visible ($\xi \lesssim R$) depends on the system size R. However, the expected exponential dependence of ξ on $k_0\ell_t$ in 2D (see Sec. V for a more precise statement) makes the condition $\xi \sim R$ accessible in realistic conditions for moderate values of $k_0\ell_t$ only.

For 2D vector waves without spatial correlation [second line of Fig. 2(a)], subradiant proximity resonances are still visible, covering now both the range of positive and negative detuning, in a similar fashion to the 3D vector case [37,47]. More importantly, localization signatures previously found at high density are now absent: decay rates near $\delta = 0$ are orders of magnitude larger than in the scalar case and IPR remain low. It has been shown numerically that such breakdown of localization at high density is due to near-field contributions of the Green's tensor $\mathbf{G}_0$ [39]. Similar observations have also been reported previously with 3D vector waves [37,38]. In 3D, near-field contributions present in the longitudinal part of $\mathbf{G}_0$ become dominant precisely in the regime of high density where the Anderson transition takes place for scalar wave. The longitudinal coupling between scatterers indirectly opens a channel for energy propagation that prevents localization to occur [37,43]. Should the same scenario apply in 2D, it would indicate the existence of a transition between a delocalized phase at large density and a localized phase at low density, albeit with an exponentially large localization length. In any case, no clear evidence of localization has been reported for 2D vector waves in resonant dipolar systems yet [39].

Finally, for 2D vector waves with substantial amount of spatial correlation [third line of Fig. 2(a)], proximity resonances have completely disappeared because the short-range repulsion of the pair potential $u(\Delta r)$ prevents scatterers to be too close to each other, as shown in Fig. 1(b). Apart from this difference, the complex spectrum is left unchanged at low density (compare TE spectra at $k_0a = 6$, for $\chi = 0$ and $\chi = 0.5$). But remarkably, at intermediate density ($k_0a = 4.5$), localization is established around $\delta = 0$ with states sharing small decay rates ($\gamma \in [10^{-12}, 10^{-6}]$) and strong confinement (IPR $\gtrsim 0.1$). In Fig. 2(c), we show a representative example of the spatial profile of localized states, with exponential shape bearing no resemblance to the delocalized profile found in the same frequency range without correlation [see Fig. 2(b)]. A systematic study reveals that all states with $\gamma \lesssim 10^{-6}$ are exponentially localized. We will provide a detailed study of the localization length ξ in Sec. V; typical distribution of ξ can be found in Appendix F. Increasing further the density makes the localization signatures disappear again (see panel at $k_0a = 2$). Hence, in finite-size systems, vector waves exhibit localization when scalar waves do not, and *vice versa*.

To further confirm the impact of correlations on 2D vector wave localization, we studied the scaling of the Thouless conductance with system size k_0R. For a fixed detuning δ, the conductance of a mode ψ_n is defined as the ratio between its linewidth γ_n and the mean spacing between neighboring normalized frequencies close to δ, $g_n = \gamma_n/\langle\delta_{n+1} - \delta_n\rangle$, where $\langle\ldots\rangle$ stands for ensemble average over different configurations. As we are interested in the lower part of the complex spectrum only, it is relevant to consider the conductance percentile g_q, defined by $q = \int_0^{g_q} dg\, p(g)$, where $p(g)$ is the probability density of g; in the following, we take

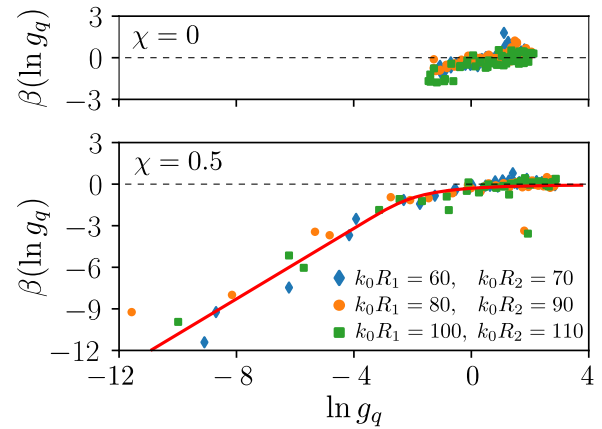
FIG. 3. Impact of spatial correlations on the scaling function $\beta(\ln g_q)$ for TE waves at $k_0a = 4.5$. The values of k_0R_1 and k_0R_2 in the legend correspond to different pairs of system sizes used to estimate $\beta(\ln g_q)$ (see text for details). For each system size, the number of disorder realizations is adjusted to have a number of eigenvalues of the order of 4×10^5. To reduce the statistical fluctuations due to the finite number of eigenvalues and the finite-difference evaluation of $\beta(\ln g_q)$, the distribution of the conductances $p(g)$ for a given value of δ includes eigenvalues in its direct vicinity $[\delta - 0.05, \delta + 0.05]$. The solid line in the bottom figure is a fit to guide the eye.

$q = 0.05$ (our results are independent of the precise value of q as long as $q \ll 1$). In Ref. [40] it has been shown that, for 3D uncorrelated systems of resonators coupled by scalar waves, the behavior of g_q is compatible with the single-parameter scaling hypothesis [31]. To investigate the validity of this hypothesis in 2D correlated materials, we evaluate the scaling function $\beta(\ln g_q) = \partial \ln g_q/\partial \ln(k_0R) \simeq [\ln g_q(R_2) - \ln g_q(R_1)]/[\ln(k_0R_2) - \ln(k_0R_1)]$, for different pairs of close system sizes (R_1, R_2) and different detuning δ. The values of $\beta(\ln g_q)$ as a function of $\ln g_q$ are reported in Fig. 3 for uncorrelated TE systems ($\chi = 0$) and correlated ones ($\chi = 0.5$), at $k_0a = 4.5$. The percentile conductance g_q of correlated materials presents a strong dependence on the system size (see Fig. 3, bottom), with large and negatives values of $\beta(\ln g_q)$ that unambiguously indicate the existence of a localized phase. In addition, all points seem to fall on a single curve, in accordance with the single-parameter scaling hypothesis. On the other hand, for uncorrelated materials, g_q remains moderate with no clear dependence on the system size (see Fig. 3, top), which corroborates the results obtained in Ref. [39].

C. Localization and density of states

To cover exhaustively the properties of TE modes, we established the phase diagram of localization in the phase space density/frequency. States that are exponentially localized in the bulk of the medium necessarily have small decay rates. Hence, a good indicator of localization is the smallest decay rate γ for fixed density and frequency, averaged over a large number of SHU configurations. It is more accurate than IPR, which can be large for states different from those localized in the bulk (see discussion below). A map of $\gamma^{\min} \equiv \langle\min(\gamma)\rangle$ is presented in Fig. 4(a) for $\chi = 0.5$. The localized phase corresponds to the smallest values of $\gamma^{\min}$ marked with warm
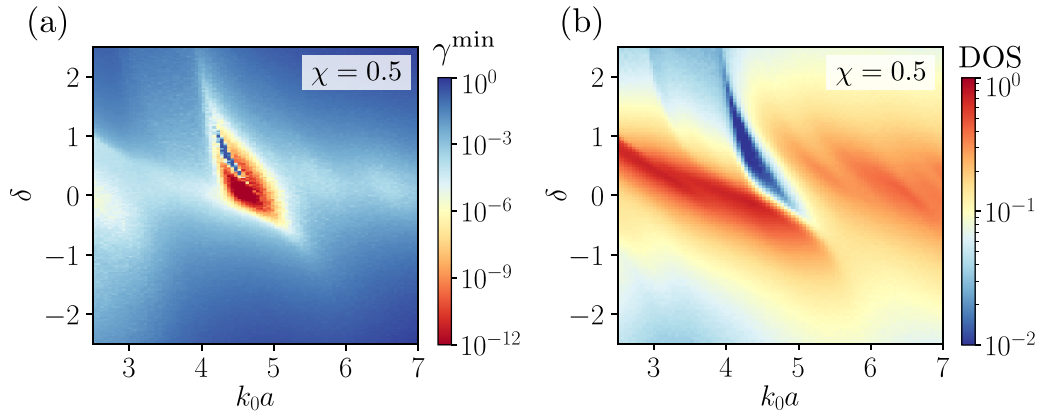
FIG. 4. (a) Map of the smallest normalized decay rate $\gamma^{\min} \equiv \langle \min(\gamma) \rangle$ in the phase space density/detuning. Small values (warm color) correspond to states localized in the bulk of the medium, associated to long lifetime. (b) Map of the normalized density of states [see Eqs. (8) and (9) for definition]. A pseudogap is found in the same phase-space domain as localized states in (a). For both maps (a) and (b), the system size is kept constant ($k_0 R = 55$) and the number of disorder realizations adjusted to have a number of eigenvalues of the order of 10^6 for each $k_0 a$.

colors ($\gamma^{\min} \lesssim 10^{-6}$); it covers an intermediate range of density corresponding to $k_0 a \in [4.2, 5.2]$. A systematic analysis for different degrees of correlation χ reveals that localization is preserved as long as $\chi \gtrsim 0.4$ with a localization island that is progressively submerged as χ is reduced. Furthermore, a similar study for TM modes (not shown) establishes localization for $k_0 a \lesssim 3$ for any χ, confirming that vector and scalar waves exhibit localization in nonoverlapping density ranges [57].

Although IPR maps in Fig. 2(a) give an indication of the spectral range covered by the resonances of the system, they do not provide information about the DOS. The latter is defined as

$$p(\omega) = \frac{1}{\mathcal{A}} \left\langle \sum_{n=1}^{\beta N} \delta(\omega - \omega_n) \right\rangle, \qquad (8)$$

where $\mathcal{A}$ is the area occupied by the disordered sample. In the thermodynamic limit ($N \to \infty$, $\mathcal{A} \to \infty$, at fixed density $\rho = N/\mathcal{A}$), almost all complex eigenvalues $\omega_n - i\Gamma_n/2$ collapse on the real axis and the definition (8) coincides with the density of modes of the Hamiltonian (4). The definition (8) is preferred to a sum of Lorentzians of widths Γ_n, because it is less sensitive to finite-size effects. The distribution $p(\omega)$ is related to the distribution of detuning $\delta = 2(\omega - \omega_0)/\Gamma_0$ as

$$p(\omega) = \frac{2\beta\rho}{\Gamma_0} p(\delta), \qquad (9)$$

where $p(\delta)$ is normalized to unity [$\int d\delta \, p(\delta) = 1$].

By computing the DOS $p(\delta)$ for different values of density, we generated the map shown in Fig. 4(b). Remarkably, the DOS exhibits a strong depletion in the domain where localization is observed in the map of $\gamma^{\min}$ [Fig. 4(a)]. A close comparison between the two maps shows a correlation between weaker features as well: When the DOS is reduced or increased, so does $\gamma^{\min}$. These observations are corroborated by similar finding for TM polarization: DOS is depleted for $k_0 a \lesssim 3$ and $\delta \gtrsim 0$ in the presence of spatial correlation, in the same phase space domain where localization occurs (not shown). Moreover, the value of the DOS in the depleted area

of Fig. 4(b) is small but finite, marking the existence of a pseudogap. The value of $p(\delta)$ inside the pseudogap is independent of the system size (at fixed density), as can be expected for states localized in the bulk of the medium. However, we also found a very thin part of the phase space where $p(\delta)$ decreases as the medium gets larger. It corresponds to the slice of modes with moderated decay rates ($\gamma \gtrsim 10^{-3}$) breaching the localization island in Fig. 4(a). The repartition of eigenvalues in the complex plane represented in Fig. 2(b) at $k_0 a = 4.5$ makes it also visible. Resonances inside this slice correspond to states mostly located at the sample boundary, and thus potentially associated to relatively large IPR. They are an artefact of the finite sample size used in simulations. In the thermodynamic limit, we expect the fraction of states in this domain to vanish, revealing a real gap. Similar observations have been made for 3D disordered crystals [35,58]. Hence, our analysis indicates that localization of vector waves occurs inside a broad pseudogap surrounding a thin gap identified in the map of $\gamma^{\min}$.

In the following sections, we will provide theoretical models that explain both the appearance of a pseudogap in the DOS and the formation of localized states in the same phase space domain. In this regard, we will justify all the differences discussed so far for TE and TM waves.

III. EFFECTIVE PHOTONIC CRYSTAL MODEL FOR THE DENSITY OF STATES

A. Density of states of crystals with large packing fraction

In the previous section, we established that a pseudogap in the DOS of TE modes forms at a relatively large degree of spatial correlation ($\chi \gtrsim 0.4$). In this regime, SHU point patterns exhibit strong local order. In Fig. 5(a), the distribution $H(r)$ of nearest neighbors at $\chi = 0.5$ appears sharply peaked near $r \sim a$ and the pair correlation function $g_2(\mathbf{r}) = 1 + h_2(\mathbf{r})$ is isotropic, with strong oscillations associated to the dominant peak of $S(\mathbf{q})$ shown in Fig. 1(c). Very similar results would be obtained with hard disks of large packing fraction instead of SHU point patterns [2,14]. When the stealth parameter is increased further and reaches $\chi \simeq 0.7 - 0.8$, the patterns crystallize in lattices with large packing fraction, such
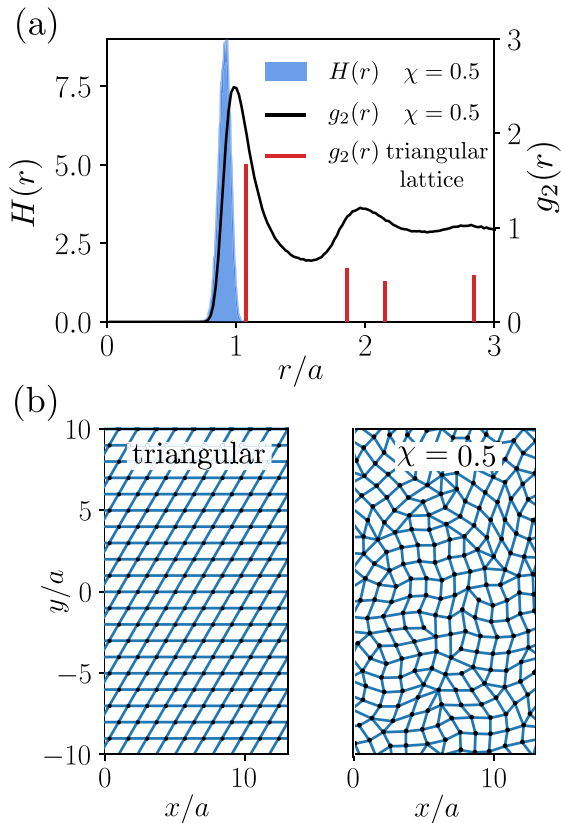
FIG. 5. (a) Nearest neighbor distribution $H(r)$ (left axis) and pair correlation function $g_2(r)$ (right axis) of a SHU configuration at $\chi = 0.5$. The function $g_2(r)$ of a triangular lattice is superimposed for comparison. (b) Connected point patterns of a triangular lattice (left) and a SHU configuration at $\chi = 0.5$ (right).

as the triangular lattice. To stress the similarities between SHU configurations at $\chi = 0.5$ and the triangular lattice, we connected points with lines to form a pattern of oblique unit cells, that preserve orientation locally. The result is compared with the tiling of the lattice with primitive cells in Fig. 5(b). In this way, a disordered pattern can be seen as an assembly

of small crystals, with orientation and lattice parameters that fluctuate while preserving a large packing fraction. Earlier papers noted that polycrystalline structures present bandgaps similar to those found in perfect crystals as long as the crystal domains are sufficiently large [14,59]. It is thus instructive to compare the DOS of SHU resonant systems with the DOS of crystals made of resonators.

Using a method detailed in Sec. III B, we first computed the map of DOS of TE modes for a triangular lattice. The result presented in Fig. 6(a) exhibits a full band gap for mostly positive detuning in a broad range of density ($k_0a \in [3.8, 6]$). The comparison with Fig. 4(b) reveals that this gap covers a phase space domain that encompasses the domain of the pseudogap found at $\chi = 0.5$. Performing a similar analysis for different oblique lattices, we found that the size of the gap decreases with the packing fraction—the largest packing fraction and gap corresponding to the triangular lattice. In particular, a minimal gap exists for all dense lattices, except for the square one (see Sec. III B for explanation). The DOS of an effective crystal mimicking the SHU pattern can be obtained by averaging the DOS over the lattice parameter space restricted to large packing fraction. As the distance between scatterers is almost constant in SHU patterns, we considered different lattices with basis vectors of equal length a^* and different relative angle θ. The range of spanned angles is chosen to maintain a packing fraction larger than 0.6, as illustrated in Fig. 7. In these crystalline point patterns, the mean distance between points is $a = a^*\sqrt{|\sin(\theta)|}$. We show in Fig. 6(b) the average DOS for a broad range of k_0a. As expected, the gap of the triangular lattice is now partially filled, revealing a strong depletion very similar to the pseudogap discussed in Fig. 4(b). This analysis corroborates the idea that SHU patterns behave as effective photonic crystals, at least as far as their DOS is concerned.

B. Theoretical predictions for Bravais lattices

Previous considerations justify a deeper theoretical treatment of crystals with large packing fraction, such as the triangular lattice. For infinite Bravais lattice, eigenstates of
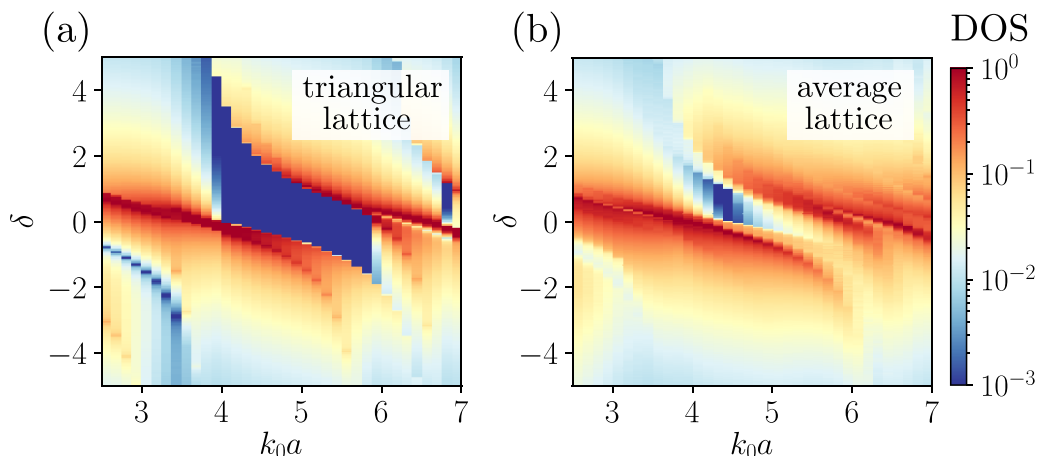

FIG. 6. (a) Normalized DOS of TE waves propagating on a triangular lattice in the phase space density/detuning. (b) Normalized DOS of TE waves, averaged over an ensemble of lattices with packing fraction superior to 0.6 (see text for details). The DOS in (b) reproduces with a good fidelity the DOS obtained with SHU configurations at $\chi = 0.5$, shown in Fig. 4(b). In particular, a pseudogap is preserved in the same range of k_0a and δ.
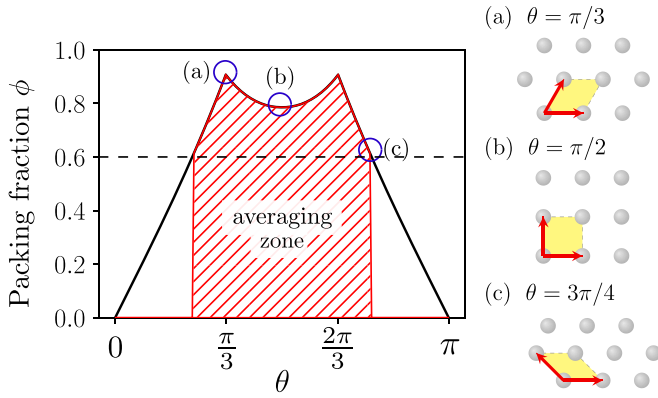
FIG. 7. Packing fraction ϕ of oblique lattices with respect to the relative angle θ between the two basis vectors. The fraction ϕ is defined as the ratio between the area of packed noninterpenetrating disks placed on the lattice and the total area. Examples of unit cells are shown on the right: triangular lattice (a) with $\phi = 0.90$, square lattice (b) with $\phi = 0.78$, and a less compact oblique lattice (c) with $\phi = 0.60$. The dashed domain shows the range of angles used to obtain the average DOS of Fig. 6(b).

the Hamiltonian (4) are Bloch modes that can be labeled by a vector $\mathbf{q}$ in the first Brillouin zone [33]. The corresponding eigenvalues are noted $\omega_{\mathbf{q}}$. Using the periodicity of the lattice, the eigenvalue problem reduces to $\det[\omega_{\mathbf{q}} \mathbb{1} - \mathcal{H}_{\mathbf{q}}(\omega_{\mathbf{q}})] = 0$, where the $\beta \times \beta$ matrix $\mathcal{H}_{\mathbf{q}}(\omega_{\mathbf{q}})$ is

$$\mathcal{H}_{\mathbf{q}}(\omega_{\mathbf{q}}) = \left(\omega_0 - i\frac{\Gamma_0}{2}\right)\mathbb{1} - \frac{\Gamma_0}{2}\tilde{\mathbb{G}}_0(\mathbf{q}, \omega_{\mathbf{q}}), \qquad (10)$$

with $\tilde{\mathbb{G}}_0(\mathbf{q}, \omega) = -4\beta(\omega/\omega_0)^2 \sum_{\mathbf{R}\neq\mathbf{0}} \mathbf{G}_0(\mathbf{R}, \omega)e^{-i\mathbf{q}\cdot\mathbf{R}}$. Since the free space Green's function $\mathbf{G}_0$ decays slowly in real space, it is not possible to perform a nearest-neighbor-type approximation of the summation involved in $\tilde{\mathbb{G}}_0(\mathbf{q}, \omega)$. Incidentally, this indicates that the tight-binding model used in Refs. [20,21] to compute the electronic DOS of amorphous semiconductors is not relevant for Hamiltonian of the form (4). In particular, such a model would be unable to predict the existence of a polaritonic gap. Using Poisson's formula instead, we convert the sum over lattice positions $\mathbf{R}$ into a sum over reciprocal lattice vectors $\mathbf{Q}$,

$$\tilde{\mathbb{G}}_0(\mathbf{q}, \omega) = -\frac{4\beta\omega^2}{\omega_0^2}\left[\rho\sum_{\mathbf{Q}}\mathbf{G}_0(\mathbf{q}-\mathbf{Q}, \omega) - \mathbf{G}_0(\mathbf{R}=\mathbf{0}, \omega)\right],$$
$$(11)$$

where the Fourier transform of the Green's function is $\mathbf{G}_0(\mathbf{q}, \omega) = 1/[(k^2 - q^2)\mathbb{1} + q^2\Delta_{\mathbf{q}}^{\parallel}\delta_{\beta,2}]$, with $\Delta_{\mathbf{q}}^{\parallel}$ the projector parallel to $\mathbf{q}$. The formulation (11) is more appropriate for computation because convergence is much faster in momentum space. The price to pay is the necessity to regularize $\mathbf{G}_0$ since the two terms in Eq. (11) diverge, whereas their difference does not [34,49]. This is done by convoluting $\mathbf{G}_0$ in real space with a function of finite but small width that smears out the divergence of $\mathrm{Re}[\mathbf{G}_0(\mathbf{R}=\mathbf{0}, \omega)]$. The regularization of $\mathbf{G}_0$ as well as the numerical procedure used to obtain, from Eqs. (10) and (11), the DOS shown in Fig. 6 are detailed in Appendix C.

Dispersion relations, $\omega_{\mathbf{q}}$ versus $\mathbf{q}$, for the triangular lattice ($\theta = \pi/3$) are shown in Fig. 8(a), along the irreducible path $\Gamma \rightarrow M \rightarrow K \rightarrow \Gamma$ of the first Brillouin zone. For consistency with previous treatments of SHU patterns, dispersion relations have been obtained, for both TM and TE polarizations, by solving the eigenvalue equation $\det[\omega_{\mathbf{q}}\mathbb{1} - \mathcal{H}_{\mathbf{q}}(\omega_{\mathbf{q}})] = 0$, with the large quality factor approximation $\mathcal{H}_{\mathbf{q}}(\omega_{\mathbf{q}}) \simeq \mathcal{H}_{\mathbf{q}}(\omega_0)$. Let us first consider the high density regime ($k_0a = 2$, top), which is the simplest to analyze. TM polarization gives a single solution $\omega_{\mathbf{q}}^0$, which exhibits a typical polaritonic dispersion relation (black dots), while TE polarization gives two solutions, labeled $\omega_{\mathbf{q}}^{\perp}$ and $\omega_{\mathbf{q}}^{\parallel}$ (red dots). These labels refer to the orientation of the corresponding eigenvectors, that can be either transverse or parallel to the wave vector $\mathbf{q}$ [see Figs. 8(b) and 8(c)]. The band $\omega_{\mathbf{q}}^{\perp}$ presents a polaritonic dispersion while $\omega_{\mathbf{q}}^{\parallel}$ is mostly flat. These different behaviors can be understood by considering the long-wavelength limit of Eq. (11), where the sum is dominated by the Fourier component $\mathbf{Q} = \mathbf{0}$,

$$\tilde{\mathbb{G}}_0(\mathbf{q}, \omega) \simeq \frac{4\beta}{(k_0a)^2}\left(\frac{k^2}{[q^2 - k^2]\mathbb{1} - q^2\Delta_{\mathbf{q}}^{\parallel}\delta_{\beta,2}} + \frac{\mathbb{1}}{2}\delta_{\beta,2}\right) - i\mathbb{1}.$$
$$(12)$$

Inserting this expression into Eq. (10), we find that the frequencies $\{\omega_{\mathbf{q}}^0, \omega_{\mathbf{q}}^{\perp}, \omega_{\mathbf{q}}^{\parallel}\}$ satisfy the following dispersion relations:

$$\omega_{\mathbf{q}}^0 = \omega_0 - \frac{\Gamma_0}{2}\frac{4}{(k_0a)^2}\frac{(\omega_{\mathbf{q}}^0/c)^2}{q^2 - (\omega_{\mathbf{q}}^0/c)^2},$$

$$\omega_{\mathbf{q}}^{\perp} = \omega_0 - \frac{\Gamma_0}{2}\frac{8}{(k_0a)^2}\left[\frac{(\omega_{\mathbf{q}}^{\perp}/c)^2}{q^2 - (\omega_{\mathbf{q}}^{\perp}/c)^2} + \frac{1}{2}\right], \quad (13)$$

$$\omega_{\mathbf{q}}^{\parallel} = \omega_0 + \frac{\Gamma_0}{2}\frac{4}{(k_0a)^2},$$

which can be interpreted as solutions of an effective medium wave equation $[-\nabla \times \nabla \times +k^2\epsilon(\omega)]E(\mathbf{r}, \omega) = \mathbf{0}$. TM plane waves of vector $\mathbf{q}$ obey the dispersion relation $q^2 = k^2\epsilon(\omega)$, where the dielectric function, $\epsilon(\omega) = 1 + \rho\alpha_e(\omega)$, is expressed in terms of an effective polarizability $\alpha_e(\omega) = 4\beta\tilde{\alpha}_e(\omega)/k_0^2$, with $\tilde{\alpha}_e(\omega) = -\Gamma_0/2(\omega - \omega_0)$. In addition, longitudinal and transverse TE solutions satisfy $\epsilon(\omega) = 0$ and $q^2 = k^2\epsilon(\omega)$, respectively, with $\epsilon(\omega) = 1 + \rho\alpha_e(\omega)/(1 - \rho\alpha_e(\omega)/2)$. Hence, in the long-wavelength limit, the crystal rigorously behaves as an homogeneous medium of effective polarizability $\alpha_e(\omega)$.

The large quality-factor approximation of Eqs. (13) amounts to replace $\omega_{\mathbf{q}}$ by ω_0 in the right-hand sides. These solutions, independent of the geometry of the Bravais lattice, are in good agreement with exact results shown in Fig. 8(a) at $k_0a = 2$. In particular, $\omega_{\mathbf{q}}^0$ and $\omega_{\mathbf{q}}^{\perp}$ diverge when they cross the light circle at $|\mathbf{q}| = k_0$, whereas $\omega_{\mathbf{q}}^{\parallel}$ does not. As a general guiding rule, divergence occurs when the polarization of the eigenstate—shown in Figs. 8(b) and 8(c) for TE waves—is tangential to light circle in the plane (q_x, q_y). Because of the polaritonic dispersion, the TM solution predicts the existence of a gap at high density, in the frequency range $\delta \in [0, 4/(k_0a)^2]$. This prediction matches with observations
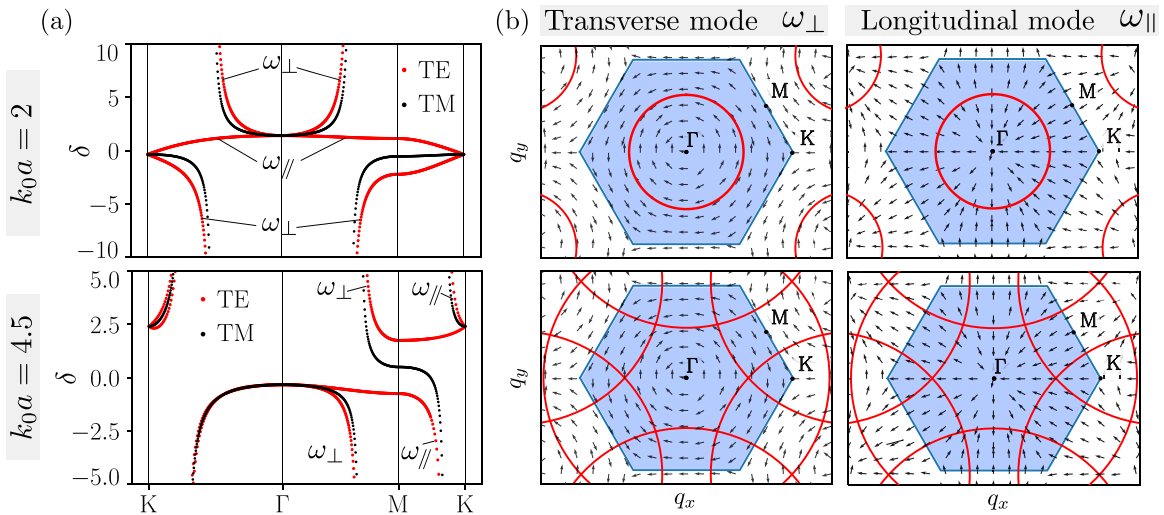
FIG. 8. (a) Photonic band structure of the triangular lattice at high density ($k_0 a = 2$, top) and moderate density ($k_0 a = 4.5$, bottom), for both TM (black) and TE (red) polarizations. For the TE case, bands are marked as transverse ($\omega_\perp$) or longitudinal ($\omega_\parallel$). (b) View of the first Brillouin zone (shaded blue), together with the light circles $|\mathbf{q}| = k_0$ and $|\mathbf{q} - \mathbf{Q}| = k_0$, at high density (top) and moderate density (bottom). Arrows represent the orientation ϵ of the eigenstates corresponding to the transverse band ($\omega_\perp$, associated to $\epsilon \perp \mathbf{q}$) and longitudinal band ($\omega_\parallel$, associated to $\epsilon \parallel \mathbf{q}$) shown in (a).

reported in Sec. II for TM waves in SHU materials. On the other hand, the TE long-wavelength approximation does not capture the closing of the gap that occurs near the point K. The approximation (13) for $\omega_{\mathbf{q}}^\parallel$ is flat, whereas the exact solution shown in Fig. 8(a) bends in the vicinity of K. The degeneracy between $\omega_{\mathbf{q}}^\perp$ and $\omega_{\mathbf{q}}^\parallel$ at point K is due to the equal contributions of the three adjacent Brillouin zones. By selecting the corresponding components [$\mathbf{Q} = \mathbf{0}$ and $\mathbf{Q}^\pm = 2\pi/a^*(1, \pm 1/\sqrt{3})$ for the triangular lattice] in Eq. (11), we find that $\tilde{\mathbb{G}}_0(\mathbf{q}, \omega)$ is proportional to the identity at K, making the distinction between longitudinal and transverse modes irrelevant. The predicted absence of gap for TE waves at high density is consistent with our findings in SHU materials [see Fig. 4(b)].

By decreasing the density of scatterers, we reduce the size of the first Brillouin zone, which may become smaller than the domain encompassed by the light circle centered in Γ. This is typically what is shown in Fig. 8(b) at $k_0 a = 4.5$. As a result, the light circles belonging to adjacent zones now intersect the first Brillouin zone. The presence or absence of gap in this regime can be found by applying the general guiding rule mentioned above. By definition, TM eigenstates are always in a plane tangential to the light circles, so that the TM band diverges when crossing both the first circle along the path $\Gamma \to M$ and the second one along the path $M \to K$ [see Fig. 8(a)]. This precludes the possibility to observe a polaritonic gap for TM polarization. On the other hand, TE eigenstates cannot be tangential to both light circles. Eigenstates associated to $\omega_{\mathbf{q}}^\perp$ are tangential to the first circle, while those associated to $\omega_{\mathbf{q}}^\parallel$ are tangential to the second one. Having a single polaritonic divergence in each of the two bands $\omega_{\mathbf{q}}^\perp$ and $\omega_{\mathbf{q}}^\parallel$ allows the formation of a TE gap, while preserving the degeneracy at points Γ and K. The validity of this reasoning suggests that the sum in Eq. (11) is dominated by the component $\mathbf{Q} = \mathbf{0}$ and its first neighbors on the reciprocal lattice. We checked numeri-

cally that a restriction of the sum to these components indeed reproduces the band structure shown in Fig. 8(a) qualitatively, with a gap found at $k_0 a = 4.5$ for TE modes only.

According to previous analysis, the TM gap observed at high density necessarily disappears when the light circle reaches the inner edge of the first Brillouin zone (point M). This occurs at $k_0 a^* = 2\pi/\sqrt{3}$, where $a^* = \sqrt{2}a/3^{1/4}$. On the contrary, a TE gap forms when the light circle reaches the outer edge (point K) and disappears as soon as the circles associated to two nonadjacent Brillouin zones meet. For the triangular lattice, a gap is thus found in the density window $k_0 a^* \in [4\pi/3, 2\pi]$. For more general oblique lattices, such as those considered in Sec. III A, criteria for the gap formation in TM and TE polarization remain the same—only the critical values of $k_0 a$ defining the gap region are modified. We have calculated analytically and represented in Fig. 9 these critical values as function of the angle θ between the two basis vectors of the direct lattice. These predictions are in excellent agreement with direct evaluation of the band structure from Eq. (10). In particular, for TE polarization, a minimal gap exists for all dense lattices because of the hexagonal shape of the Brillouin zone. The only exception is the square lattice, which has a square Brillouin zone and for which the conditions for gap opening and closing are the same.

Our detailed examination of the band structure for arbitrary oblique lattice reveals that geometrical arguments involving light circles and the shape of the Brillouin zone accurately capture the main features of the DOS at high or moderate density. In particular, these arguments explain the robustness of the TE gap, even after averaging over an ensemble of lattices mimicking SHU pattern, as shown in Fig. 6(b). However, they hold for SHU patterns with large degree of correlation χ only. In the following section, we aim at characterizing theoretically the continuous evolution of $p(\delta)$ from white-noise disorder ($\chi = 0$) to strongly correlated SHU patterns ($\chi \sim 0.5$).
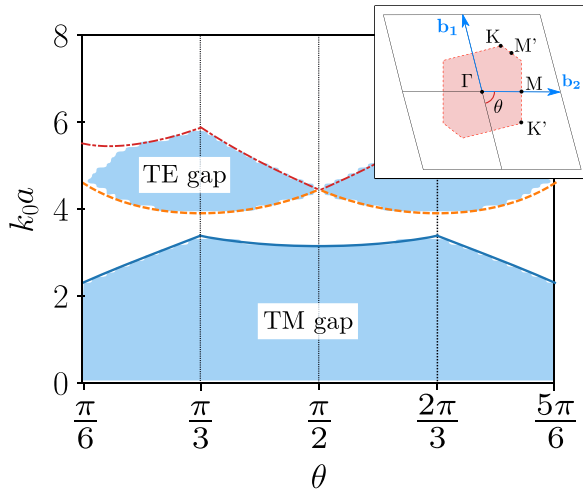
FIG. 9. Critical values $k_0 a$ defining the gap regions as function of the direct lattice angle θ. Lines are theoretical predictions and filled areas cover the gaps found numerically from the band structure. The TM gap disappears when the light circle reaches the closer inner edge of the first Brillouin zone (see inset), either in M or M' depending on θ. It corresponds to the critical value $k_0 a^* = \min(\pi/|\sin\theta|, \pi\sqrt{2 - 2\cos\theta}/|\sin\theta|)$, where $a^* = a/\sqrt{|\sin\theta|}$ is the distance between unit cells of the direct lattice. The TE gap opens when the light circle reaches the outer edges in K and K', which corresponds to $k_0 a^* = \pi/(1 + \cos\theta)|\sin(\theta/2)|$; it closes for $k_0 a^* = \min(\pi/|\sin(\theta/2)|, \pi|\sin\theta|/\sqrt{5 - 4\cos\theta})$, when the light circles associated to two nonadjacent Brillouin zones first meet, either in M or M'. TM and TE gaps are found in nonoverlapping regimes of density. The range of density for the existence of the TE gap is maximal for the triangular lattice ($\theta = \pi/3$) and minimal for the square lattice ($\theta = \pi/2$).

IV. MICROSCOPIC SCATTERING MODEL FOR THE DENSITY OF STATES

Our objective is to evaluate the DOS of the effective Hamiltonian $\mathcal{H}(\omega_0)$ defined in Eq. (4), at finite density $\rho = N/\mathcal{A}$ and arbitrary χ, in the limit of large system size ($N \to \infty$, $\mathcal{A} \to \infty$). This DOS is related to the pdf of eigenvalues Λ_n of the Green's matrix $\tilde{\mathbb{G}}_0(\omega_0)$ through a simple rescaling. When increasing the area $\mathcal{A}$ occupied by the scatterers, most of the eigenvalues Λ_n that lie in the upper part of the complex plane ($\mathrm{Im}\Lambda_n > -1$) progressively collapse towards the line $\mathrm{Im}\Lambda = -1$, so that the imaginary part of most of the eigenvalues of $\mathcal{H}(\omega_0)$ become vanishingly small while remaining negative. As a result, the distribution of detuning $\delta = 2(\omega - \omega_0)/\Gamma_0$ defined through Eqs. (8) and (9) can be written in the form

$$p(\delta) = -\frac{1}{\pi\beta N}\mathrm{Im}\left\langle\mathrm{Tr}\left[\frac{1}{(\delta + i)\mathbb{1} + \tilde{\mathbb{G}}_0(\omega_0)}\right]\right\rangle, \quad (14)$$

where Tr stands for the trace of a matrix. The average trace involved in Eq. (14) may be evaluated theoretically by generalizing the Euclidean random matrix theory framework developed in Refs. [36,51,60] to correlated arrangements of scatterers. This is not the strategy adopted in the following, where we wish to establish a clear connection with quantities commonly manipulated in mesoscopic physics theory, such as the collective **T** operator or the self-energy $\mathbf{\Sigma}$ [27,61].

The collective **T** operator in an ensemble of N scatterers is the sum of all possible elastic scattering sequences experienced by waves of frequency ω [27],

$$\mathbf{T}(\omega) = \sum_l \mathbf{t}_l + \sum_l \sum_{m \neq l} \mathbf{t}_l \mathbf{G}_0(\omega)\mathbf{t}_m$$
$$+ \sum_l \sum_{n \neq l} \sum_{m \neq n} \mathbf{t}_l \mathbf{G}_0(\omega)\mathbf{t}_n \mathbf{G}_0(\omega)\mathbf{t}_m + \cdots, \quad (15)$$

where $\mathbf{t}_l$ is the **t** operator of the point-like scatterer l located in $\mathbf{r}_l$, of amplitude $t(\omega) = -k^2\alpha(\omega) = -4\beta k^2\tilde{\alpha}(\omega)/k_0^2$. In the momentum representation, the series (15) is recast as

$$\mathbf{T}(\mathbf{q}, \omega) = \frac{4\beta}{\mathcal{A}}\sum_{l=1}^{N}\sum_{m=1}^{N}\left[\frac{1}{(\delta + i)\mathbb{1} + \tilde{\mathbb{G}}_0(\omega_0)}\right]_{lm} e^{-i\mathbf{q}\cdot(\mathbf{r}_l - \mathbf{r}_m)}. \quad (16)$$

This expression applies for resonators of large quality factor described by the polarizability (3). Since only the components $l = m$ contribute significantly to Eq. (16) in the limit $q \to \infty$, we establish the following connection between $p(\delta)$ in Eq. (14) and the average **T** operator:

$$p(\delta) = -\frac{1}{4\pi\beta^2\rho}\lim_{q \to \infty}\mathrm{ImTr}[\langle\mathbf{T}(\mathbf{q}, \omega)\rangle]. \quad (17)$$

Hence, we are left with the evaluation of $\langle\mathbf{T}(\mathbf{q}, \omega)\rangle$. Note that this expression of $p(\delta)$ does not include the DOS of free-propagating light. The latter is due to the resonances of the free space Green's function $\mathbf{G}_0(\omega)$ itself, which are lost as soon as we replace $\mathbf{G}_0(\omega)$ by $\mathbf{G}_0(\omega_0)$. In the case of crystals, we did not need such assumption, so that the free space dispersion relation, as well as the DOS of free-propagating light was recovered in the limit of vanishing density [see the discussion below Eq. (13)].

The average collective **T** operator is conveniently expressed in terms of the self-energy $\mathbf{\Sigma}(\mathbf{q}, \omega)$ as

$$\langle\mathbf{T}(\mathbf{q}, \omega)\rangle = \frac{\mathbf{\Sigma}(\mathbf{q}, \omega)}{\mathbb{1} - \mathbf{G}_0(\mathbf{q}, \omega_0)\mathbf{\Sigma}(\mathbf{q}, \omega)}. \quad (18)$$

By definition, $\mathbf{\Sigma}(\mathbf{q}, \omega)$ is the sum of all possible irreducible scattering sequences contained in the expansion of $\langle\mathbf{T}(\mathbf{q}, \omega)\rangle$. In the following, we restrict our analysis to the regime of moderate density ($k_0 a \gtrsim 3$), where it is legitimate to perform an expansion of the self-energy in density ρ. By averaging Eq. (15) and keeping all irreducible diagrams up to the second order in ρ, we get [62]

$$\mathbf{\Sigma}(\mathbf{q}, \omega) = \rho\, t(\omega)\mathbb{1} + \rho^2 t(\omega)^2 \int d\mathbf{r}\, h_2(\mathbf{r})\mathbf{G}_0(\mathbf{r}, \omega_0)e^{-i\mathbf{q}\cdot\mathbf{r}} + \rho^2 t(\omega)^3 \int d\mathbf{r}\, [1 + h_2(\mathbf{r})]\frac{\mathbf{G}_0^2(\mathbf{r}, \omega_0)}{\mathbb{1} - t(\omega)^2\mathbf{G}_0^2(\mathbf{r}, \omega_0)}$$

$$+ \rho^2 t(\omega)^4 \int d\mathbf{r}\, [1 + h_2(\mathbf{r})]\frac{\mathbf{G}_0^3(\mathbf{r}, \omega_0)}{\mathbb{1} - t(\omega)^2\mathbf{G}_0^2(\mathbf{r}, \omega_0)}e^{-i\mathbf{q}\cdot\mathbf{r}}. \quad (19)$$
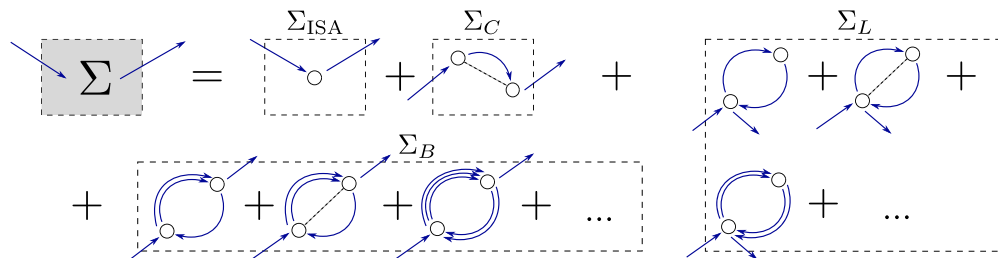
FIG. 10. Pictorial representation of the scattering sequences included in the self-energy $\boldsymbol{\Sigma}$. Open circles represent scatterers, arrows account for field propagation through $\mathbf{G}_0$, and dashed line connecting scatterers stand for the spatial correlation function h_2. Diagrams are classified into four classes discussed in the text. The pseudogap found in the DOS $p(\delta)$ for strongly correlated systems is triggered by the destructive interference between the independent scattering contribution, $\boldsymbol{\Sigma}_{\mathrm{ISA}}$, and the scattering loops involving two spatially correlated scatterers, $\boldsymbol{\Sigma}_L$.

The four terms of the expression (19) are represented schematically in Fig. 10. The first one $\boldsymbol{\Sigma}_{\mathrm{ISA}}$ is the independent scattering approximation of the self-energy, which is the only relevant term in the limit of dilute uncorrelated system. By keeping this first order in density in Eq. (17), we find that the DOS $p(\delta)$ takes a Lorentzian profile,

$$p(\delta) = \frac{1}{\pi} \frac{1}{1 + \delta^2}, \tag{20}$$

both for TM and TE waves. This result is in excellent agreement with numerical simulations at $\chi = 0$ in the dilute limit $k_0 a \gg 1$ (results not shown). The second term in Eq. (19), noted $\boldsymbol{\Sigma}_C$ in Fig. 10, corresponds to scattering by two correlated scatterers, while the two last terms, $\boldsymbol{\Sigma}_L$ and $\boldsymbol{\Sigma}_B$, are recurrent scattering contributions involving pairs of scatterers; $\boldsymbol{\Sigma}_L$ stands for scattering loops, which end where they start, and $\boldsymbol{\Sigma}_B$ represents boomerang-like sequences in which the last scatterer differs from the first one. For TM waves, $\boldsymbol{\Sigma}_C$ and $\boldsymbol{\Sigma}_B$ do not contribute to $p(\delta)$ because they vanish in the limit $q \to \infty$. On the contrary, for TE waves, they contribute to $p(\delta)$ through the singularity $\delta(\mathbf{r})\mathbb{1}/2k_0^2$ of $\mathbf{G}_0(\mathbf{r}, \omega_0)$. The corresponding weight of $\boldsymbol{\Sigma}_C + \boldsymbol{\Sigma}_B$ is $-\rho^2 t(\omega)^2 \mathbb{1}/2k_0^2$, irrespectively of the amplitude of the correlation h_2. This term, which slightly red-shifts $p(\delta)$ by an amount $\Delta\delta \simeq -4/(k_0 a)^2$ in 2D, is the so-called Lorentz-Lorenz correction to the DOS, discussed in Refs. [63,64] for 3D uncorrelated media. The only contribution in Eq. (19) that gives a dependence of $p(\delta)$ on the degree of spatial correlation is thus the loop term $\boldsymbol{\Sigma}_L$.

We have represented in Fig. 11(a) maps of the DOS $p(\delta)$ of TE waves in the regime of moderate density $k_0 a \in [2.5, 7]$, for two degrees of spatial correlation, $\chi = 0$ (top) and $\chi = 0.5$ (bottom). Numerical distributions obtained from the diagonalization of the Hamiltonian (4) (left panels) are compared with the theoretical prediction (17), evaluated at the second order in density with Eqs. (18) and (19) (right panels). Details regarding the explicit analytical computation of Eq. (17) and Eq. (19) are given in Appendix D. Good agreement between numerics and theory is found over a broad range of density and detuning, all the way from uncorrelated system ($\chi = 0$) to strongly correlated one ($\chi = 0.5$). This confirms the validity of the connection established in Eq. (17) between $p(\delta)$ and the average collective $\mathbf{T}$ operator.

Figure 11(b) shows cuts of the two maps along the line $k_0 a = 4.5$. In the absence of spatial correlation (top), $p(\delta)$ differs slightly from the Lorentzian profile (20) found in the dilute limit (dashed line). In particular, the loop correction

$\boldsymbol{\Sigma}_L$ is responsible for an antisymmetric contribution to $p(\delta)$ through $\mathrm{Im}[t(\omega)^3]$, which blue-shifts the maximum of $p(\delta)$ and creates a depletion at $\delta < 0$. On the contrary, for a large degree of correlation (bottom), $\boldsymbol{\Sigma}_L$ is responsible for a dip in the DOS at $\delta > 0$, which coincides with the pseudogap found in simulations. To understand the origin of this dip, it is sufficient to consider the single loop approximation $\boldsymbol{\Sigma}_L \simeq \rho^2 t(\omega)^3 \int d\mathbf{r}\, g_2(\mathbf{r}) \mathbf{G}_0^2(\mathbf{r}, \omega_0)$. At $\chi = 0.5$, the pair correlation function $g_2(\mathbf{r}) = 1 + h_2(\mathbf{r})$ is zero for $r \lesssim a$ and presents a dominant peak at $r \simeq a$. As a result, most of the scatterers involved in a scattering loop are separated by a distance a. For $\delta \gtrsim 0$ and $k_0 a = 4.5$, the phase accumulated along a scattering loop of length a is opposite to the phase of single scattering, so that $\boldsymbol{\Sigma}_{\mathrm{ISA}}$ and $\boldsymbol{\Sigma}_L$ are of opposite sign and interfere destructively. In other words, our analysis reveals that the pseudogap is due to a robust interference between two types of scattered waves, and not to an interference between the field illuminating each particle and the scattered field, as it has been proposed in Ref. [17]. It also shows that the absence of a gap in the regime of high density for TE polarization is due to the longitudinal part of $G_0(\mathbf{q}, \omega)$, which is in line with the predictions made in Sec. III B. Contrary to what has been put forward in Ref. [17], there is no need for extra Mie-type resonance to fill the gap found for TM waves. The fact that our theory does not reproduce quantitatively the pseudogap at moderate density is attributed to the density expansion of $\boldsymbol{\Sigma}$ performed above. We expect the agreement with numerical DOS to get better when including scattering loops made of more than two spatially correlated scatterers.

Our theoretical treatment of the DOS not only provides explicit expressions of $p(\delta)$ for any χ, but also indicates which microscopic scattering mechanisms contribute to the formation of the pseudogap in correlated materials, and what should be the profile of the spatial correlation function to make the pseudogap prominent.

V. LOCALIZATION LENGTH IN CORRELATED RESONANT SYSTEMS

We found in Sec. II C that the formation of a pseudogap in the DOS $p(\delta)$ of correlated materials is concomitant to a modification of the eigenstates of $\mathcal{H}(\omega_0)$. States near the band edges become exponentially localized in the bulk of the medium, and, as a result, acquire very long life times in finite-size samples. Here we want to establish, in an explicit manner, the connection between $p(\delta)$ and the localization properties
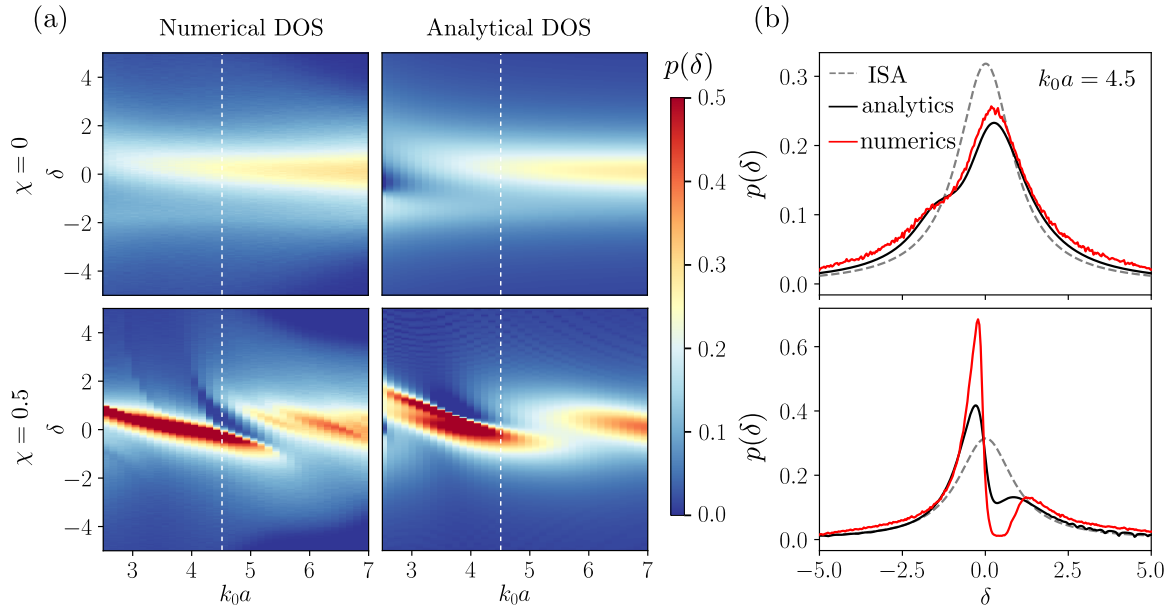
FIG. 11. (a) Comparison between the numerical DOS $p(\delta)$ of TE waves (left) and the theoretical prediction (17), including recurrent scattering and spatial correlation at the second order in density (right). Good agreement is found for $k_0 a \gtrsim 3$, without (top) and with (bottom) spatial correlation. (b) Cuts along the line $k_0 a = 4.5$ of the maps shown in (a). The Lorentzian profile (20) for dilute uncorrelated system is shown with a dashed line for reference. Numerical results shown in (a) and (b) have been obtained with a system size $k_0 R = 55$ and a number of disorder realizations adjusted to have $\sim 10^6$ eigenvalues for each $k_0 a$.

of $\mathcal{H}(\omega_0)$. To characterize the latter, it is custom to consider the spatial properties of the intensity associated to the field operator $\mathcal{G}(\omega) = 1/[\omega \mathbb{1} - \mathcal{H}(\omega_0)]$ [27]. The mean intensity is defined as

$$I^{\alpha\gamma}(\mathbf{R}, \Omega) = \langle \mathcal{G}_{ij}^{\alpha\gamma}(\omega^+) \mathcal{G}_{ij}^{\alpha\gamma}(\omega^-)^* \rangle, \tag{21}$$

where $\omega^\pm = \omega \pm \Omega/2$, (i, j) are positions indices with $\mathbf{r}_i = \mathbf{r}_j + \mathbf{R}$, and (α, γ) refer to output and input polarization channels. Using Eq. (16), we can also express the intensity in terms of the collective $\mathbf{T}$ operator,

$$I^{\alpha\gamma}(\mathbf{R}, \Omega) \propto \langle \mathbf{T}_{ij}^{\alpha\gamma}(\omega^+) \mathbf{T}_{ij}^{\alpha\gamma}(\omega^-)^* \rangle, \tag{22}$$

where $\mathbf{T}_{ij}^{\alpha\gamma}(\omega) = ([(\delta + i)\mathbb{1} + \tilde{\mathbb{G}}_0(\omega_0)]^{-1})_{ij}^{\alpha\gamma}$.

One common way to find the expression of the correlator (22) is to write a Bethe-Salpeter equation for $\langle \mathbf{TT}^\dagger \rangle$ and compute its irreducible vertex at a given order in density using the expansion (15). In the long time limit ($\Omega \to 0$) and large-scale limit ($R \gg \ell_t$), $I^{\alpha\gamma}(\mathbf{R}, \Omega)$ is dominated by the scalar mode of the Bethe-Salpeter equation, which is independent of the polarization channels: $I^{\alpha\gamma}(\mathbf{R}, \Omega) \equiv I(\mathbf{R}, \Omega)$ [61]. In addition, in the regime of weak scattering ($k\ell_s \gg 1$, where ℓ_s is the scattering mean free path discussed below), the mean intensity effectively obeys a diffusion equation. In the Fourier domain, it reads

$$(DQ^2 - i\Omega)I(\mathbf{Q}, \Omega) = 0, \tag{23}$$

with $I(\mathbf{Q}, \Omega)$ the Fourier transform of $I(\mathbf{R}, \Omega)$. If localization corrections are ignored, the diffusion coefficient D for 2D waves reduces to

$$D_0 = \frac{\ell_t v_E}{2}, \tag{24}$$

where $\ell_t = \ell_s/(1 - g)$ is the transport mean free path, g the scattering anisotropy factor, and v_E the energy velocity. In an ensemble of scatterers with large quality factors, v_E is much smaller than c, because of the long time ($\sim \Gamma_0^{-1}$) spent for each scattering event: $v_E \simeq \Gamma_0 \ell_s$ [19]. This definition of ℓ_t includes all possible scattering events up to the second order in density (see Appendix E for a precise definition and calculation), except those that contribute to long-range cooperons. The effect of the latter, which are responsible for localization in infinite system, are incorporated below. We stress that the result (24) includes the vectorial nature of the problem at hand, in the sense that the explicit expressions of ℓ_s and g, which involve the self-energy and the irreducible vertex, depend on it [2,64]. But it neglects other genuinely new vector effects that may show up in the regime of large density, where near-field radiation carried by the longitudinal part of the Green's tensor $\mathbf{G}_0(\mathbf{q}, \omega)$ becomes dominant. Specifically, it was put forward recently that the interference between the longitudinal and transverse waves contribute to the diffusive current and thus increase the value of the diffusion coefficient [43]. In the regime of moderate density we are interested in ($k_0 a \gtrsim 4$), we checked explicitly that removing the longitudinal part of $\mathbf{G}_0(\mathbf{q}, \omega)$ in the definition of the Hamiltonian (4) does not change our findings for TE waves: both pseudogap and localization signatures shown in Fig. 4 are preserved quantitatively.

In infinite 2D systems, localization corrections to the result (24) cannot be ignored. When a pair of complex conjugated fields evolves along a diffusive path, there is a high probability to form a scattering loop in which the two fields propagate along the same path but in opposite directions. Accounting for these loops (cooperons) self-consistently leads to a profound modification of D, which becomes solution of the

equation [32]

$$D = D_0 - DP_0, \qquad (25)$$

where P_0 is the return probability to the origin by diffusion,

$$P_0 = \frac{1}{\pi p(\omega)} \int \frac{d\mathbf{Q}}{(2\pi)^2} \frac{1}{DQ^2 - i\Omega}. \qquad (26)$$

This expression explicitly depends on the DOS $p(\omega)$ of the Hamiltonian (4), defined in Eq. (8). The integral that appears in the expression of P_0 diverges at large Q, because the diffusion process breaks down at distance shorter than $\sim \ell_t$. By introducing a cutoff $q_{max} = 1/\ell_t$, we get

$$P_0 = \frac{1}{(2\pi)^2 p(\omega) D} \ln\left(1 + \frac{iD}{\Omega \ell_t^2}\right). \qquad (27)$$

In the stationary limit $\Omega \to 0^+$, the solution D of Eq. (25) is thus purely imaginary. It reads

$$D = -i\Omega \xi^2, \qquad (28)$$

where ξ is a characteristic length defined as

$$\xi = \ell_t e^{2\pi^2 p(\omega) D_0}. \qquad (29)$$

With the result (28), the stationary solution of Eq. (23) becomes $I(\mathbf{R}) \sim e^{-R/\xi}$, so that ξ can be interpreted as the localization length. By inserting the expressions of D_0 and $p(\omega)$, given by Eqs. (24) and (9), into the formal solution (29), we finally get

$$\xi = \ell_t e^{2\pi^2 \beta \rho \ell_t \ell_s p(\delta)}, \qquad (30)$$

which applies both for TM ($\beta = 1$) and TE ($\beta = 2$) waves. As mentioned above, this prediction has been demonstrated in the regime of moderate density ($k_0 a \gtrsim 4$), where the contribution of the longitudinal part of the Green's tensor to the diffusive current is negligible.

To analyze the main features of the result (30), we need to specify the expression of ℓ_s. In the absence of absorption, ℓ_s characterizes the exponential extinction of the ballistic light inside the disordered medium. At second order in density, its inverse takes the form

$$\frac{1}{\ell_s} = \frac{-\text{Im}[\Sigma^{\perp}(q = k_0, \omega)]}{\omega_0 / v_{\varphi}}, \qquad (31)$$

where $v_{\varphi} = c[1 + \text{Re}\Sigma_{\text{ISA}}^{\perp}(\omega)]$ is the phase velocity and $\Sigma^{\perp}(q = k_0, \omega)$ is the transverse part of $\Sigma(\mathbf{q}, \omega)$ given in Eq. (19), evaluated on the shell $|\mathbf{q}| = k_0$. Its explicit analytical expression is given in Appendix D. The result (31) is based on the on-shell approximation that breaks down at large density. In that case, the dielectric constant of the effective medium is nonlocal and the extinction of the ballistic component is no more exponential. We checked numerically that this occurs in our systems for $k_0 a \lesssim 4.6$.

The comparison of Eqs. (17) and (31) shows that $p(\delta)$ and ℓ_s, whose product appears in the expression (30) of the localization length, are both expressed in terms of $\Sigma(\mathbf{q}, \omega)$. The first one however depends on both the transverse and longitudinal parts of $\Sigma(\mathbf{q}, \omega)$, evaluated at $q \to \infty$ instead of $q = k_0$. As a consequence, the term $\Sigma_B(\mathbf{q}, \omega)$ contributes to ℓ_s but not to $p(\delta)$. The only case where the product $\rho \ell_s p(\delta)$ is independent of detuning and density is the one of dilute systems
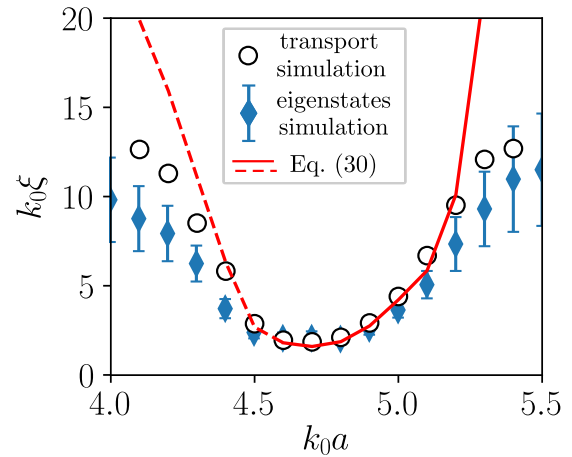

FIG. 12. Comparison between the localization length ξ obtained from transport simulation (open circles) and eigenstate profile (filled diamonds), with the formula (30) (solid and dashed line), in a ensemble of correlated resonant dipoles ($\chi = 0.5$, $\delta = 0$), illuminated with TE polarization. The localization length is strongly reduced when the DOS $p(\delta)$ is depleted. Equation (30) has been evaluated with numerical values of $p(\delta)$ and ℓ_s. For $k_0 a < 4.6$, reliable values of ℓ_s cannot be found, which is attributed to nonlocality of the effective dielectric constant (see text for details); the value of ℓ_s obtained at $k_0 a = 4.6$ is thus extrapolated to get ξ at lower $k_0 a$ (dashed line). Details about transport simulation and eigenstate analysis are given in Appendix F.

($k_0 a \gg 1$), for which $\Sigma(\mathbf{q}, \omega) \simeq \Sigma_{\text{ISA}}(\omega)\mathbb{1}$ is independent of $\mathbf{q}$. Then, Eq. (30) reduces to

$$\xi \simeq \ell_t e^{\frac{\pi k_0 \ell_t}{2}}, \qquad (32)$$

which is the commonly used expression for the localization length in 2D [24,32]. We stress that the result (32) is not accurate as soon as spatial correlation and recurrent scattering become important. In particular, for TE waves at $\chi = 0.5$, we find that the frequency profile of $p(\delta)$ is strongly asymmetric [see Fig. 11(b)], whereas the theoretical prediction (31) gives an almost symmetric profile of ℓ_s versus δ (result not shown). Furthermore, the dependence of $p(\delta)$ on $k_0 a$ is strongly nonmonotonic [see Fig. 11(a)], whereas Eq. (31) yields to a monotonic increase of ℓ_s with $k_0 a$. In this situation, the product $\rho \ell_s p(\delta)$ is not constant and the approximation (32) of Eq. (30) does not hold.

To test the validity on the prediction (30), and in particular its explicit dependance on $p(\delta)$, we first computed numerically the values of ℓ_s and ξ in the TE polarization at $\chi = 0.5$. For this purpose, we illuminated a disordered slab of thickness L made of resonant dipoles and studied the dependence on L of the mean-field intensity measured in transmission, $|\langle \mathbf{E}(L)\rangle|^2$, as well as the mean of the logarithm of the intensity, $\langle \ln[|\mathbf{E}(L)|^2]\rangle$. Details of the calculation are given in Appendix F. We also checked that the values of ξ found in this way are compatible with a direct fit of the exponential profile of the localized eigenstates of $\mathcal{H}(\omega_0)$; typical profile of the eigenstates and distribution of ξ are shown in Appendix F. Second, we estimated ℓ_t by computing theoretically the irreducible vertex in the presence of spatial correlation at second order in density. This amounts to gener-

alize the results of Ref. [64] to 2D correlated systems. After a lengthy calculation presented in Appendix E, we found that the scattering anisotropy factor g is of the order of ~ 0.1 for $k_0 a \in [4, 5.5]$, so that $\ell_t \simeq 1.1 \ell_s$. In Fig. 12, we compare the numerical values of ξ with the formula (30) evaluated with the numerical values of ℓ_s and $p(\delta)$, in the range of $k_0 a$ where $p(\delta)$ exhibits a pseudogap. We find that ξ is strongly reduced in this density window, confirming the critical dependence of ξ on $p(\delta)$. Hence, formula (30) justifies quantitatively why localized states form when the DOS is depleted.

VI. CONCLUSIONS

We have demonstrated in this paper that spatial correlations in disordered systems profoundly modify the properties of 2D vector waves, by inducing pseudogap in the DOS as well as spatial localization. To explain these results, we established a general formula for the DOS, Eq. (17), that we expressed at the second order in density in terms of the pair correlation function $g_2(\mathbf{r}) = h_2(\mathbf{r}) + 1$. This expression captures the impact of the disorder-to-order transition on the DOS. Strong spatial correlations force the scatterers to be at a well defined distance from each other, which allows for efficient destructive interference between elementary scattering processes involving one and two scatterers, in the density window $k_0 a \in [4.2, 5.2]$. Hyperuniformity ($\lim_{\mathbf{q} \to 0} S(\mathbf{q}) = 0$) is not a requisite condition for this process. It can be realized with hard disk systems as well, since the latter present very similar pair correlation function for the right choice of packing fraction [14].

We also developed a complementary model for the DOS based on an effective-crystal representation. This model captures the fundamental difference between scalar and vector waves in the regime of high density. At $k_0 a \lesssim 3$, longitudinal and transverse TE modes interact to prevent the formation of a polaritonic gap similar to the one formed by TM modes. On the other hand, at $k_0 a \gtrsim 4$, transverse and longitudinal modes exhibit independent polaritonic dispersions that result in a TE gap, whereas TM waves support a double polaritonic dispersion that closes the gap. By analyzing the mechanisms responsible for these band structures, we were able to predict accurately the nonoverlapping regimes of density where TE and TM gaps are observed in strongly correlated materials. As a byproduct, our analysis also reveals that we cannot describe correlated resonant media by means of a nearest-neighbor tight-binding Hamiltonian, as Weaire and Thorpe did for amorphous semiconductors [20,21].

Finally, we proved that the localization length ξ in 2D correlated systems takes the general form (30). This result explicitly shows that spatial correlations can deeply affect localization, not only by modifying the scattering mean free path ℓ_s and the scattering anisotropy factor g as found numerically in Ref. [24], but also by depleting the DOS $p(\delta)$. In this way, we explained why it is so difficult to observe localization of TE modes in uncorrelated media of finite size and why spatial correlations turn out to be a powerful knob to reach localization. Our predictions for $p(\delta)$ and ξ are supported quantitatively by extensive numerical simulations of wave propagation in hyperuniform systems.

By providing theoretical grounds as well microscopic mechanisms for the emergence of photonic gap and localization, we clarify recent experimental and numerical findings that put forward the role of short-range order for these processes [10–12,14,26]. We also establish the possibility to induce localization for 2D TE waves propagating through in-plane dipole excitations, which has not been explored experimentally so far. Finally, our theoretical treatments of the DOS and localization can, in principle, be extended to 3D systems. Although the possibility to propagate along a third dimension evidently leads to qualitative different behavior, the role of spatial correlations and the microscopic mechanisms responsible for $p(\delta)$ and ξ are formally the same as in 2D. Hence, we think that our paper will help to identify the key structural ingredients that affect significantly wave propagation in 2D and 3D strongly correlated materials. Even more generally, we stress that the theoretical results (17,18, 19) and (30), for the DOS and the localization length respectively, hold for arbitrary Hamiltonian of the form (4), where $\tilde{\mathbb{G}}_0(\omega)$ could describe any type of long-range excitation exchange between different sites. They are therefore potentially relevant for a broad class of systems in photonics and condensed matter physics, ranging from connected photonic networks [13] to those described by effective spin interactions [65].

APPENDIX A: ELECTROMAGNETIC GREEN'S FUNCTION AND GREEN'S MATRIX IN 2D

Throughout this article, we have considered a translationally invariant medium along one direction so that the usual 3×3 Green's tensor splits into two independent block elements, a scalar one in the TM polarization when the excitation lies along the invariance direction, and a 2×2 block for the TE polarization with a field perpendicular to it. For the sake of simplicity both operators will be denoted $\mathbf{G}_0$. For TM polarization, $\mathbf{G}_0$ is such that

$$[\nabla^2 + k^2]\mathbf{G}_0(\mathbf{r} - \mathbf{r}', \omega) = \delta(\mathbf{r} - \mathbf{r}'), \quad (A1)$$

$$\mathbf{G}_0(\mathbf{R}, \omega) = -\frac{i}{4} \mathrm{H}_0^{(1)}(kR), \quad (A2)$$

where $\mathrm{H}_\alpha^{(1)}$ is the Hankel function of the first kind and order α. Similarly in the TE polarization the Green's tensor $\mathbf{G}_0$ reads

$$[-\boldsymbol{\nabla} \times \boldsymbol{\nabla} \times + k^2]\mathbf{G}_0(\mathbf{r} - \mathbf{r}', \omega) = \mathbb{1}\delta(\mathbf{r} - \mathbf{r}'), \quad (A3)$$

$$\mathbf{G}_0(\mathbf{R}, \omega) = -\frac{i}{4} \mathrm{PV}\left[\left(\mathbb{1} - \frac{\mathbf{R} \otimes \mathbf{R}}{R^2}\right) \mathrm{H}_0^{(1)}(kR)\right.$$
$$\left. -\left(\mathbb{1} - 2\frac{\mathbf{R} \otimes \mathbf{R}}{R^2}\right) \frac{\mathrm{H}_1^{(1)}(kR)}{kR}\right] + \frac{\delta(\mathbf{R})}{2k^2}\mathbb{1}. \quad (A4)$$
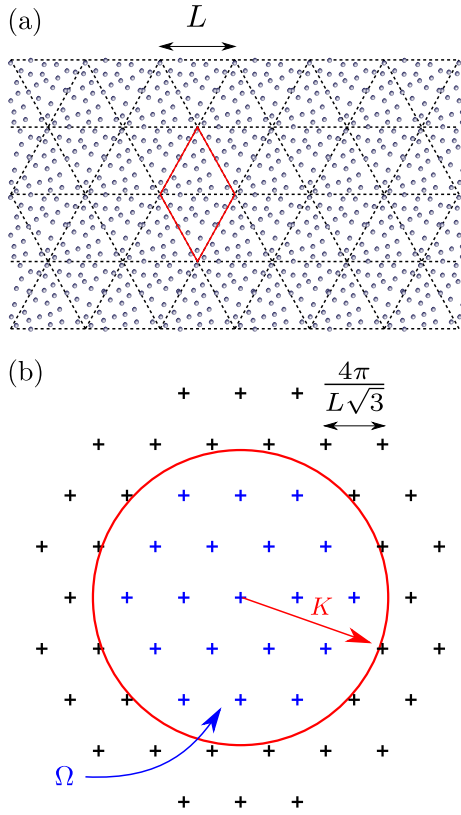
(a)

(b)

FIG. 13. (a) Periodic system considered to generate stealth hyperuniform point patterns. (b) Ensemble Ω of points of the reciprocal space where the structure factor have to be optimized.

APPENDIX B: HYPERUNIFORM PATTERN GENERATION AND PROPERTIES

In this Appendix, we focus on the process used to generate stealth hyperuniform point patterns. This process is adapted from Refs. [14,55,66–68]. SHU patterns are such that the structure factor $\tilde{S}(\mathbf{q})$ vanishes in a domain $|\mathbf{q}| < K$. Numerically, only a finite number of points can be manipulated. To mimic an infinite medium, we thus divide the space into identical unitary cells. A square lattice is often too restrictive since it forces the point pattern to crystallize into a square lattice at large χ. For that reason, we have chosen a triangular (or hexagonal) lattice [see Fig. 13(a)].

The induced periodicity implies that the structure factor vanishes for all $\mathbf{q}$ except the ones lying on the reciprocal lattice. The problem of generating a SHU pattern reduces now to an optimization process to minimize the structure factor for all $\mathbf{q} \in \Omega$ where Ω is the intersection of the reciprocal lattice and the domain $|\mathbf{q}| < K$ [see Fig. 13(b)]. This can be translated into the determination of point positions that minimizes the potential

$$U(\{\mathbf{r}_j\}) = \sum_{\mathbf{q} \in \Omega} \left| \sum_j \exp(i\mathbf{q} \cdot \mathbf{r}_j) \right|^2. \tag{B1}$$

In practice, the first guess is a fully random configuration of points (Poisson point pattern) on which a conjugate gradient method is applied which leads to a SHU point pattern. De-

pending on the intended use, the unitary cell structure is then scaled and cropped to obtain a SHU point pattern inside a disk of radius R and density $\rho = a^{-2}$.

Finally, we note that the structure factors $\tilde{S}(\mathbf{q}) = \sum_{i,j} e^{i\mathbf{q} \cdot (\mathbf{r}_i - \mathbf{r}_j)} / N$ and $S(\mathbf{q}) = 1 + \rho h_2(\mathbf{q})$ are linked through the relation

$$S(\mathbf{q}) = \tilde{S}(\mathbf{q}) - 4\pi^2 \rho \delta(\mathbf{q}) \tag{B2}$$

in an infinite medium (we have to remove the forward-scattering component). In a finite-sized medium, this relation becomes [55]

$$S(\mathbf{q}) = \tilde{S}(\mathbf{q}) - \frac{N-1}{\mathcal{A}^2} |\Theta(\mathbf{q})|^2, \tag{B3}$$

where $\mathcal{A}$ is the area occupied by the scattering medium and $\Theta(\mathbf{q})$ is the Fourier transform of the function

$$\Theta(\mathbf{r}) = \begin{cases} 1 & \text{if } \mathbf{r} \in \mathcal{A}, \\ 0 & \text{otherwise.} \end{cases} \tag{B4}$$

APPENDIX C: REGULARIZATION OF THE CRYSTALLINE HAMILTONIAN AND LARGE WAVELENGTH EXPANSION

To construct the dispersion relation in infinite crystals, we recall the Hamiltonian of Eq. (10) expressed in term of Bloch waves

$$\mathcal{H}_{\mathbf{q}}(\omega_{\mathbf{q}}) = \left(\omega_0 - i\frac{\Gamma_0}{2} \right)\mathbb{1} - \frac{\Gamma_0}{2}\tilde{\mathbb{G}}_0(\mathbf{q}, \omega_{\mathbf{q}}), \tag{C1}$$

with $\tilde{\mathbb{G}}_0(\mathbf{q}, \omega) = -4\beta(\omega/\omega_0)^2 \sum_{\mathbf{R} \neq \mathbf{0}} \mathbf{G}_0(\mathbf{R}, \omega)e^{-i\mathbf{q} \cdot \mathbf{R}}$. Following the procedure of Refs. [34,49], we want to convert the sum over the lattice into a sum in reciprocal space. Poisson's formula requires the evaluation of the Green's function at its singularity. This has been circumvented by regularizing the Green's function using a Gaussian cut-off in momentum space, which smoothen the real space divergence at the origin. Explicitly we used the following relation derived in Ref. [49]

$$\sum_{\mathbf{R} \neq \mathbf{0}} \mathbf{G}_0(\mathbf{R}, \omega)e^{-i\mathbf{q} \cdot \mathbf{R}} \simeq e^{\frac{k^2 b^2}{2}} \rho \sum_{\mathbf{Q}} \mathbf{G}_0^*(\mathbf{Q} - \mathbf{q}, \omega)$$
$$- \mathbf{G}_0^*(\mathbf{R} = \mathbf{0}, \omega), \tag{C2}$$

where the regularized Green's function in momentum space takes the form

$$\mathbf{G}_0^*(\mathbf{q}, \omega) = \mathbf{G}_0(\mathbf{q}, \omega)e^{-\frac{q^2 b^2}{2}}, \tag{C3}$$

where b is the regularization parameter. Using Eqs. (C2) and (C3), we can rewrite Eq. (11) as a sum of finite terms

$$\tilde{\mathbb{G}}_0(\mathbf{q}, \omega) = -\frac{4\beta\omega^2}{\omega_0^2} e^{\frac{k^2 b^2}{2}} \left[\frac{1}{V_L} \sum_{\mathbf{Q}} \mathbf{G}_0^*(\mathbf{q} - \mathbf{Q}, \omega) \right.$$
$$\left. - \mathbf{G}_0^*(\mathbf{R} = \mathbf{0}, \omega) \right], \tag{C4}$$

which becomes independent of b for $b \ll a$. For the TM polarization, the last term of Eq. (C4) reads

$$\mathbf{G}_0^*(\mathbf{R} = \mathbf{0}, \omega) = -\frac{i}{4} \int d\mathbf{r} \, \mathrm{H}_0^{(1)}(kr) \frac{e^{-\frac{r^2}{2b^2}}}{2\pi b^2}$$

$$\underset{kb \ll 1}{\simeq} -\frac{1}{\pi}\left[\gamma + \ln\left(\frac{k^2 b^2}{2}\right)\right] - \frac{i}{4}. \quad (C5)$$

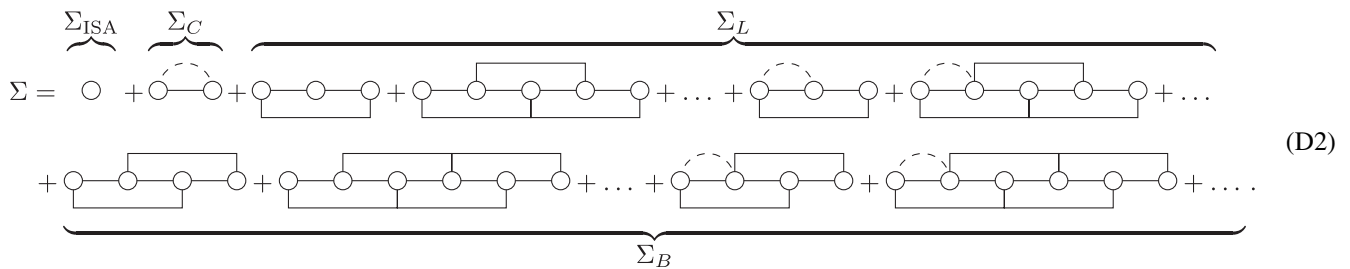Here the Hankel function has been approximated at small values by

$$\mathrm{H}_0^{(1)}(x) \underset{x \ll 1}{\simeq} 1 + \frac{i}{\pi}\left[2\gamma + \ln\left(\frac{x^2}{4}\right)\right], \quad (C6)$$

where γ is the Euler's constant. In the TE polarization, using $\int_0^{2\pi} d\theta \, (\mathbb{1} - \hat{\mathbf{r}} \otimes \hat{\mathbf{r}}) = \pi \mathbb{1}$ and $\int_0^{2\pi} d\theta \, (\mathbb{1} - 2\hat{\mathbf{r}} \otimes \hat{\mathbf{r}}) = 0$ where $\hat{\mathbf{r}} = \mathbf{r}/r$, we get

$$\mathbf{G}_0^*(\mathbf{R}=\mathbf{0}, \omega) = -\frac{i\pi \mathbb{1}}{4} \int_0^\infty dr \, r \, \mathrm{H}_0^{(1)}(kr) \frac{e^{-\frac{r^2}{2b^2}}}{2\pi b^2} + \frac{\mathbb{1}}{4\pi k^2 b^2}$$

$$\underset{kb \ll 1}{\simeq} -\frac{\mathbb{1}}{2\pi}\left[\gamma + \ln\left(\frac{k^2 b^2}{2}\right)\right]$$

$$- \mathbb{1}\left(\frac{i}{8} - \frac{1}{4\pi k^2 b^2}\right). \quad (C7)$$

In the long-wavelength limit ($qa \ll 1$), Eq. (12) can be obtained from Eq. (C4), in the same fashion as in Ref. [49] for 3D crystals. A more direct way is to go back to Eq. (C1) and to compute $\sum_{\mathbf{R} \neq 0} \mathbf{G}_0(\mathbf{R}) e^{-i\mathbf{q} \cdot \mathbf{R}}$ in the high-density limit, which gives

$$\sum_{\mathbf{R} \neq \mathbf{0}} \mathbf{G}_0(\mathbf{R}, \omega) e^{i\mathbf{q} \cdot \mathbf{R}} \underset{qa \ll 1}{\simeq} \frac{1}{a^2} \int d\mathbf{R} \, \mathbf{G}_0(\mathbf{R}, \omega) e^{-i\mathbf{q} \cdot \mathbf{R}}$$

$$- i \, \mathrm{Im}[\mathbf{G}_0(\mathbf{R} = \mathbf{0}, \omega)]$$

$$- \frac{1}{a^2} \int_{\delta\mathcal{A}} d\mathbf{R} \, \mathrm{Re}[\mathbf{G}_0(\mathbf{R}, \omega)]$$

$$\simeq \frac{1}{a^2} \mathbf{G}_0(\mathbf{q}, \omega) + \mathbb{1}\left(\frac{i}{4} - \frac{\delta_{\beta,2}}{2k^2 a^2}\right)$$

$$+ \mathbb{1} \frac{\delta\mathcal{A}}{a^2}(2 - \delta_{\beta,2})\left[\frac{2\gamma - 1 + \ln(k^2 \delta\mathcal{A}/4\pi)}{8\pi}\right], \quad (C8)$$

where $\delta\mathcal{A}$ is a small surface enclosing the origin. Taking the limit $\delta\mathcal{A} \to 0$, we obtain Eq. (12).

For small enough b/a, the Hamiltonian computed with Eq. (C4) is independent of the regularization parameter b. In practice, we set $b/a = 0.01$, and truncate the sum over the reciprocal lattice by keeping $\mathbf{Q}$, which satisfy $|\mathbf{q} - \mathbf{Q}| \lesssim 7/b$. In order to generate dispersion relations such as shown in Fig. 9, the Hamiltonian is then diagonalized for $\mathbf{q}$ belonging to an irreducible path of the first Brillouin zone. Moreover, the numerical density of states $p(\delta)$ shown in Fig. 6 is obtained by sampling an irreducible area of the first Brillouin zone and counting the number of resonances per unit frequency.

APPENDIX D: COMPUTATION OF THE SELF-ENERGY AND $p(\delta)$

In order to evaluate Eq. (17), it is convenient to use the decomposition $\mathbf{\Sigma}(\mathbf{q}, \omega) = \Sigma^\perp(\mathbf{q}, \omega)\mathbf{\Delta}_{\mathbf{q}}^\perp + \Sigma^\parallel(\mathbf{q}, \omega)\mathbf{\Delta}_{\mathbf{q}}^\parallel$ and $\mathbf{G}_0(\mathbf{q}, \omega) = G_0^\perp(\mathbf{q}, \omega)\mathbf{\Delta}_{\mathbf{q}}^\perp + G_0^\parallel(\mathbf{q}, \omega)\mathbf{\Delta}_{\mathbf{q}}^\parallel$, where $\mathbf{\Delta}_{\mathbf{q}}^\perp$ and $\mathbf{\Delta}_{\mathbf{q}}^\parallel$ are the projectors perpendicular and parallel to $\mathbf{q}$. We get

$$p(\delta) = -\frac{1}{4\pi\beta\rho} \lim_{q \to \infty} \mathrm{Im}\left[\frac{\Sigma^\perp(\mathbf{q}, \omega)}{1 - G_0^\perp(\mathbf{q}, \omega)\Sigma^\perp(\mathbf{q}, \omega)} + \frac{\Sigma^\parallel(\mathbf{q}, \omega)}{1 - G_0^\parallel(\mathbf{q}, \omega)\Sigma^\parallel(\mathbf{q}, \omega)}\right]. \quad (D1)$$

A first simplification comes from the fact that $G_0^\perp(\mathbf{q}, \omega) \to 0$ when $q \to \infty$, reducing the first term to the numerator $\Sigma^\perp$. Then, we take into account all scattering processes involving two different scatterers in the computation of the transverse $[\Sigma^\perp(\mathbf{q}, \omega)]$ and longitudinal $[\Sigma^\parallel(\mathbf{q}, \omega)]$ self-energies. This corresponds to a second-order expansion in density and gives the following diagrams:

$$(D2)$$

This diagrammatic representation is similar to the one shown in Fig. 10. Circles represent scattering events and horizontal-solid lines are for the free space Green's functions connecting these scattering events. Also, disorder correlations are denoted by dashed-curved lines and identical scatterers (recurrent scattering) are linked by solid upper and lower lines. Eq. (D2) takes the compact form

$$\mathbf{\Sigma}(\mathbf{q}, \omega) = \mathbf{\Sigma}_{\mathrm{ISA}}(\mathbf{q}, \omega) + \mathbf{\Sigma}_C(\mathbf{q}, \omega)$$
$$+ \mathbf{\Sigma}_L(\mathbf{q}, \omega) + \mathbf{\Sigma}_B(\mathbf{q}, \omega), \quad (D3)$$

where

$$\boldsymbol{\Sigma}_{\mathrm{ISA}}(\mathbf{q}, \omega) = \rho\, t(\omega)\mathbb{1}, \tag{D4}$$

$$\boldsymbol{\Sigma}_C(\mathbf{q}, \omega) = \rho^2 t(\omega)^2 \int d\mathbf{r}\, h_2(\mathbf{r})\mathbf{G}_0(\mathbf{r}, \omega_0)e^{-i\mathbf{q}\cdot\mathbf{r}}, \tag{D5}$$

$$\boldsymbol{\Sigma}_L(\mathbf{q}, \omega) = \rho^2 t(\omega)^3 \int d\mathbf{r}\, [1 + h_2(\mathbf{r})]\frac{\mathbf{G}_0^2(\mathbf{r}, \omega_0)}{\mathbb{1} - t(\omega)^2\mathbf{G}_0^2(\mathbf{r}, \omega_0)}, \tag{D6}$$

$$\boldsymbol{\Sigma}_B(\mathbf{q}, \omega) = \rho^2 t(\omega)^4 \int d\mathbf{r}\, [1 + h_2(\mathbf{r})]\frac{\mathbf{G}_0^3(\mathbf{r}, \omega_0)e^{-i\mathbf{q}\cdot\mathbf{r}}}{\mathbb{1} - t(\omega)^2\mathbf{G}_0^2(\mathbf{r}, \omega_0)}. \tag{D7}$$

Let us first consider $\boldsymbol{\Sigma}_C$. To compute this term, we expand the Green's function given by Eq. (A4) into its transverse and longitudinal projections in real space and its singular part as

$$\mathbf{G}_0(\mathbf{r}, \omega) = G_0^t(r, \omega)\boldsymbol{\Delta}_r^\perp + G_0^l(r, \omega)\boldsymbol{\Delta}_r^\| + \frac{\delta(\mathbf{R})}{2k^2}\mathbb{1} \tag{D8}$$

where $\boldsymbol{\Delta}_r^\perp$ ($\boldsymbol{\Delta}_r^\|$) is the transverse (longitudinal) projector with respect to $\mathbf{r}$. Using the relations

$$\int_0^{2\pi} d\theta\, \boldsymbol{\Delta}_r^\perp e^{-i\mathbf{q}\cdot\mathbf{r}} = 2\pi\left[\mathrm{J}_0(qr) - \frac{\mathrm{J}_1(qr)}{qr}\right]\boldsymbol{\Delta}_q^\perp$$
$$+ 2\pi\frac{\mathrm{J}_1(qr)}{qr}\boldsymbol{\Delta}_q^\|, \tag{D9}$$

$$\int_0^{2\pi} d\theta\, \boldsymbol{\Delta}_r^\| e^{-i\mathbf{q}\cdot\mathbf{r}} = 2\pi\frac{\mathrm{J}_1(qr)}{qr}\boldsymbol{\Delta}_q^\perp$$
$$+ 2\pi\left[\mathrm{J}_0(qr) - \frac{\mathrm{J}_1(qr)}{qr}\right]\boldsymbol{\Delta}_q^\|, \tag{D10}$$

where $\mathrm{J}_0(x)$ and $\mathrm{J}_1(x)$ are Bessel functions of the first kind, we find that $\boldsymbol{\Sigma}_C$ takes the form

$$\boldsymbol{\Sigma}_C(\mathbf{q}, \omega) = \Sigma_C^\perp(\mathbf{q}, \omega)\boldsymbol{\Delta}_q^\perp + \Sigma_C^\|(\mathbf{q}, \omega)\boldsymbol{\Delta}_q^\| + \Sigma_C^{\mathrm{LL}}(\mathbf{q}, \omega)\mathbb{1}, \tag{D11}$$

with

$$\Sigma_C^\perp(\mathbf{q}, \omega) = 2\pi\rho^2 t(\omega)^2 \int_0^\infty dr\, r\, h_2(r)\left\{G_0^t(r, \omega_0)\left[\mathrm{J}_0(qr) - \frac{\mathrm{J}_1(qr)}{qr}\right] + G_0^l(r, \omega_0)\frac{\mathrm{J}_1(qr)}{qr}\right\}, \tag{D12}$$

$$\Sigma_C^\|(\mathbf{q}, \omega) = 2\pi\rho^2 t(\omega)^2 \int_0^\infty dr\, r\, h_2(r)\left\{G_0^t(r, \omega_0)\frac{\mathrm{J}_1(qu)}{qr} + G_0^l(r, \omega_0)\left[\mathrm{J}_0(qr) - \frac{\mathrm{J}_1(qu)}{qr}\right]\right\}, \tag{D13}$$

$$\Sigma_C^{\mathrm{LL}}(\mathbf{q}, \omega) = \frac{\rho^2 t(\omega)^2 h_2(0)}{2k_0^2}. \tag{D14}$$

Here the last term $\Sigma_C^{\mathrm{LL}}(\mathbf{q}, \omega)$ is due to the singular part of the Green's function.

In the same way we can write the loop term $\boldsymbol{\Sigma}_L$ in the form

$$\boldsymbol{\Sigma}_L(\mathbf{q}, \omega) = \Sigma_L^\perp(\mathbf{q}, \omega)\boldsymbol{\Delta}_q^\perp + \Sigma_L^\|(\mathbf{q}, \omega)\boldsymbol{\Delta}_q^\| + \Sigma_L^{\mathrm{LL}}(\mathbf{q}, \omega)\mathbb{1}. \tag{D15}$$

The first two terms follow from the decomposition

$$\frac{\mathbb{1}}{\mathbb{1} - t(\omega)^2\mathbf{G}_0^2(\mathbf{r}, \omega_0)} = \sum_{j=0}^\infty [t(\omega)^2\mathbf{G}_0(\mathbf{r}, \omega_0)^2]^j = \sum_{j=0}^\infty [t(\omega)^2 G^t(r, \omega_0)^2]^j \boldsymbol{\Delta}_r^\perp + [t(\omega)^2 G^l(r, \omega_0)^2]^j \boldsymbol{\Delta}_r^\|$$

$$= \frac{1}{1 - t(\omega)^2 G_0^t(r, \omega_0)^2}\boldsymbol{\Delta}_r^\perp + \frac{1}{1 - t(\omega)^2 G_0^l(r, \omega_0)^2}\boldsymbol{\Delta}_r^\|. \tag{D16}$$

Taking the limit $\mathbf{q} \to \mathbf{0}$ in Eqs. (D9) and (D10), we get $\int_0^{2\pi} d\theta\, \boldsymbol{\Delta}_r^\perp = \int_0^{2\pi} d\theta\, \boldsymbol{\Delta}_r^\| = \pi\mathbb{1}$, which leads to

$$\Sigma_L^\perp(\mathbf{q}, \omega) = \Sigma_L^\|(\mathbf{q}, \omega) = \pi\rho^2 t(\omega)^3 \int_0^\infty dr\, r[1 + h_2(r)]\left[\frac{G_0^t(r, \omega_0)^2}{1 - t(\omega)^2 G_0^t(r, \omega_0)^2} + \frac{G_0^l(r, \omega_0)^2}{1 - t(\omega)^2 G_0^l(r, \omega_0)^2}\right]. \tag{D17}$$

In addition, the contribution of the singular part of $\mathbf{G}_0(\mathbf{r}, \omega)$ to $\boldsymbol{\Sigma}_L(\mathbf{q}, \omega)$ vanishes thanks to a simplification of the δ terms appearing in Eq. (D6), $\Sigma_L^{\mathrm{LL}}(\mathbf{q}, \omega) = 0$.

Finally, we consider the boomerang term $\boldsymbol{\Sigma}_B$ that we write in the form

$$\boldsymbol{\Sigma}_B(\mathbf{q}, \omega) = \Sigma_B^\perp(\mathbf{q}, \omega)\boldsymbol{\Delta}_q^\perp + \Sigma_B^\|(\mathbf{q}, \omega)\boldsymbol{\Delta}_q^\| + \Sigma_B^{\mathrm{LL}}(\mathbf{q}, \omega)\mathbb{1}. \tag{D18}$$

Using Eqs. (D16) and (D9), we obtain

$$\Sigma_B^\perp(\mathbf{q}, \omega) = 2\pi\rho^2 \int_0^\infty dr\, r[1 + h_2(r)]\left\{\frac{t(\omega)^4 G_0^{t3}(r, \omega_0)}{1 - t(\omega)^2 G_0^{t2}(r, \omega_0)}\left[\mathrm{J}_0(qr) - \frac{\mathrm{J}_1(qr)}{qr}\right] + \frac{t(\omega)^4 G_0^{l3}(r, \omega_0)}{1 - t(\omega)^2 G_0^{l2}(r, \omega_0)}\frac{\mathrm{J}_1(qr)}{qr}\right\}, \tag{D19}$$

$$\Sigma_B^\|(\mathbf{q}, \omega) = 2\pi\rho^2 \int_0^\infty dr\, r[1 + h_2(r)]\left\{\frac{t(\omega)^4 G_0^{t3}(r, \omega_0)}{1 - t(\omega)^2 G_0^{t2}(r, \omega_0)}\frac{\mathrm{J}_1(qr)}{qr} + \frac{t(\omega)^4 G_0^{l3}(r, \omega_0)}{1 - t(\omega)^2 G_0^{l2}(r, \omega_0)}\left[\mathrm{J}_0(qr) - \frac{\mathrm{J}_1(qr)}{qr}\right]\right\}, \tag{D20}$$

$$\Sigma_B^{\mathrm{LL}}(\mathbf{q}, \omega) = -\frac{\rho^2 t(\omega)^2(1 + h_2(0))}{2k_0^2}. \tag{D21}$$
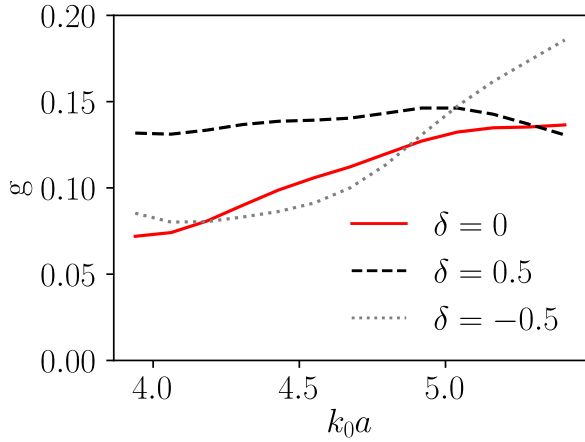
FIG. 14. Anisotropy factor g for TE waves propagating in a highly correlated ensemble of resonators ($\chi = 0.5$), with detuning $\delta = 0$ (solid-red line), $\delta = 0.5$ (dashed-black line), and $\delta = -0.5$ (dotted-grey line). The anisotropy factor fluctuates between 0.05 and 0.2 in the density window where localization is prominent (see Fig. 12).

It is interesting to note that the two terms coming from the singular part of the Green's function simplify, which gives

$$\Sigma^{\mathrm{LL}}(\mathbf{q}, \omega) = \Sigma_C^{\mathrm{LL}}(\mathbf{q}, \omega) + \Sigma_B^{\mathrm{LL}}(\mathbf{q}, \omega) = -\frac{\rho^2 t(\omega)^2}{2k_0^2}. \quad (D22)$$

At first order, this contribution is identical to the one we would obtain considering point-like repulsion between scatterers and known as Lorentz-Lorenz correction.

In the evaluation of the density of states, only the large wave-vector limit participates hence removing the contribution of Σ_B and the wave-vector-dependent part of Σ_C. The only term, which needs to be computed numerically is Σ_L. The first integrand involving G_0^t is regular at the origin, but not absolutely convergent for large arguments. Indeed, $k_0 r G_0^{t2}(r, \omega_0)$ is equivalent to $i \exp[2ik_0 r]/8\pi$. The integral can be computed nonetheless by setting a cut-off r_c in the following way [69]:

$$\int_0^\infty dr\, r[1 + h_2(r)] \frac{G_0^t(r, \omega_0)^2}{1 - t(\omega)^2 G_0^t(r, \omega_0)^2}$$
$$= \int_0^{r_c} dr\, r[1 + h_2(r)] \frac{G_0^t(r, \omega_0)^2}{1 - t(\omega)^2 G_0^t(r, \omega_0)^2}$$
$$+ \int_{r_c}^\infty dr\, r[1 + h_2(r)] \frac{G_0^t(r, \omega_0)^2}{1 - t(\omega)^2 G_0^t(r, \omega_0)^2}. \quad (D23)$$
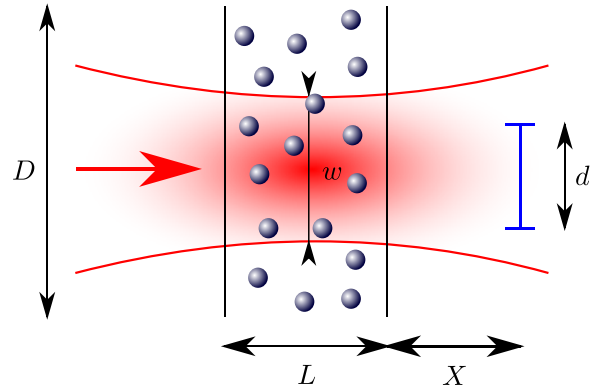

FIG. 15. Numerical setup used to estimate ℓ_s and ξ. Red: Gaussian beam illuminating the medium. Blue: Screen on which the transmitted field is computed.

For a large enough value of r_c, the first integral is computed numerically and the second one is approximated by

$$\int_{r_c}^\infty dr\, r G_0^t(r, \omega_0)^2 \simeq \frac{i}{8\pi k_0} \int_{r_c}^\infty \exp[2ik_0 r] dr = \frac{\exp[2ik_0 r_c]}{16\pi k_0^2}. \quad (D24)$$

The final result (D23) is independent of r_c.

APPENDIX E: COMPUTATION OF THE ANISOTROPY FACTOR g FOR TE WAVES

The transport mean free path ℓ_t can be linked to the scattering mean free path ℓ_s through the anisotropy factor g. In 2D, it is given by

$$\frac{1}{\ell_t} = \frac{1 - g}{\ell_s} = \frac{\langle (1 - \hat{\mathbf{q}} \cdot \hat{\mathbf{q}}') U^\perp(k_0 \hat{\mathbf{q}}, k_0 \hat{\mathbf{q}}', \omega) \rangle_{\hat{\mathbf{q}}'}}{4k_0}, \quad (E1)$$

where $\hat{\mathbf{q}} = \mathbf{q}/q$ with $q = k_0$, $\langle \cdots \rangle_{\hat{\mathbf{q}}'}$ denotes an average over the direction of $\hat{\mathbf{q}}'$, and $U^\perp(\mathbf{q}, \mathbf{q}', \omega) = \sum_{i,j,k,l} \Delta_{\mathbf{q},ij}^\perp U_{ij,kl}(\mathbf{q}, \mathbf{q}', \omega) \Delta_{\mathbf{q}',kl}^\perp$ is the transverse part of the irreducible vertex $\mathbf{U}(\mathbf{q}, \mathbf{q}', \omega)$ of the Bethe-Salpeter equation [27]. Here, we are specifically interested in the anisotropy factor, which reads

$$g = \ell_s \frac{\langle \hat{\mathbf{q}} \cdot \hat{\mathbf{q}}' \, U^\perp(k_0 \hat{\mathbf{q}}, k_0 \hat{\mathbf{q}}', \omega) \rangle_{\hat{\mathbf{q}}'}}{4k_0}, \quad (E2)$$

where ℓ_s is given by Eq. (31). At the second order in density, the angular average in the numerator of Eq. (E2) has nonzero contributions from the following diagrams [62,64]:

$$(E3)$$

$$+ \quad + \quad + \quad + \ldots + \text{c.c.} \tag{E4}$$

$$\mathbf{U}_B = \quad + \quad + \quad + \quad + \ldots + \text{c.c.} \tag{E5}$$

where the notations are identical to those used in Eq. (D2), with the upper and lower lines accounting for the propagating field and its conjugate, respectively. Explicitly, the first term reads

$$\mathbf{U}_C(\mathbf{q}, \mathbf{q}', \omega) = \rho^2 |t(\omega)|^2 h_2(\mathbf{q} - \mathbf{q}')\mathbb{1}, \tag{E6}$$

so that the angular average of its transverse part can be written in the form

$$\langle \hat{\mathbf{q}} \cdot \hat{\mathbf{q}}' U_C^{\perp}(\mathbf{q}, \mathbf{q}', \omega) \rangle_{\hat{\mathbf{q}}'} = \rho |t(\omega)|^2 \int_0^{2\pi} \frac{d\theta}{2\pi} h_2(2q|\sin(\theta/2)|) \cos^3 \theta. \tag{E7}$$

The loop and boomerang contributions, $\mathbf{U}_L$ and $\mathbf{U}_B$, are

$$\mathbf{U}_L(\mathbf{q}, \mathbf{q}', \omega) = \rho^2 |t(\omega)|^2 \int d\mathbf{r}[1 + h_2(r)]e^{i(\mathbf{q}-\mathbf{q}')\cdot\mathbf{r}} \left\{ \frac{\mathbb{1}}{[\mathbb{1} - t(\omega)^2 \mathbf{G}_0(\mathbf{r}, \omega_0)^2] \otimes [\mathbb{1} - t(\omega)^2 \mathbf{G}_0(\mathbf{r}, \omega_0)^2]^*} - \mathbb{1} \right\}, \tag{E8}$$

$$\mathbf{U}_B(\mathbf{q}, \mathbf{q}', \omega) = \rho^2 |t(\omega)|^4 \int d\mathbf{r}[1 + h_2(r)]e^{i(\mathbf{q}+\mathbf{q}')\cdot\mathbf{r}} \frac{\mathbf{G}_0(\mathbf{r}, \omega_0) \otimes \mathbf{G}_0^*(\mathbf{r}, \omega_0)}{[\mathbb{1} - t(\omega)^2 \mathbf{G}_0(\mathbf{r}, \omega_0)^2] \otimes [\mathbb{1} - t(\omega)^2 \mathbf{G}_0(\mathbf{r}, \omega_0)^2]^*}. \tag{E9}$$

The angular integrations over the directions of $\mathbf{r}$ and $\hat{\mathbf{q}}$ that appear in $\langle \hat{\mathbf{q}} \cdot \hat{\mathbf{q}}' U_L^{\perp}(\mathbf{q}, \mathbf{q}', \omega) \rangle_{\hat{\mathbf{q}}'}$ and $\langle \hat{\mathbf{q}} \cdot \hat{\mathbf{q}}' U_B^{\perp}(\mathbf{q}, \mathbf{q}', \omega) \rangle_{\hat{\mathbf{q}}'}$ can be performed using the decomposition (D8) and the relation (D16). After a lengthy calculation, we find

$$\langle \hat{\mathbf{q}} \cdot \hat{\mathbf{q}}' U_L^{\perp}(\mathbf{q}, \mathbf{q}', \omega) \rangle_{\hat{\mathbf{q}}'} = -\rho^2 |t(\omega)|^2 \int_0^{\infty} dr \, r[1 + h_2(r)] \left\{ A(qr) \left| \frac{1}{1 - t(\omega)^2 G_0^t(r, \omega_0)^2} \right|^2 + B(qr) \left| \frac{1}{1 - t(\omega)^2 G_0^l(r, \omega_0)^2} \right|^2 \right.$$
$$\left. + 2C(qr) \text{Re} \left[\left(\frac{1}{1 - t(\omega)^2 G_0^t(r, \omega_0)^2} \right) \left(\frac{1}{1 - t(\omega)^2 G_0^l(r, \omega_0)^2} \right)^* \right] - D(qr) \right\}, \tag{E10}$$

$$\langle \hat{\mathbf{q}} \cdot \hat{\mathbf{q}}' U_B^{\perp}(\mathbf{q}, \mathbf{q}', \omega) \rangle_{\hat{\mathbf{q}}'} = \rho^2 |t(\omega)|^4 \int_0^{\infty} dr \, r[1 + h_2(r)] \left\{ A(qr) \left| \frac{G_0^t(r, \omega_0)}{1 - t(\omega)^2 G_0^t(r, \omega_0)^2} \right|^2 + B(qr) \left| \frac{G_0^l(r, \omega_0)}{1 - t(\omega)^2 G_0^l(r, \omega_0)^2} \right|^2 \right.$$
$$\left. + 2C(qr) \text{Re} \left[\left(\frac{G_0^t(r, \omega_0)}{1 - t(\omega)^2 G_0^t(r, \omega_0)^2} \right) \left(\frac{G_0^l(r, \omega_0)}{1 - t(\omega)^2 G_0^t(r, \omega_0)^2} \right)^* \right] \right\}, \tag{E11}$$

where $A(x) = -2\pi [J_2(x) - xJ_1(x)]^2/x^2$, $B(x) = C(x) = -2\pi J_2(x)^2/x^2$, $D(x) = A(x) + 3B(x)$, and $J_1(x)$ and $J_2(x)$ are Bessel functions of the first kind. We note that the remaining

integration over r is not convergent for $r \to \infty$ because of the term $rA(qr)|G_0^t(r, \omega_0)|^2 \sim \cos(kr)^2/r$. We regularize this logarithmic divergence by replacing the free space Green's
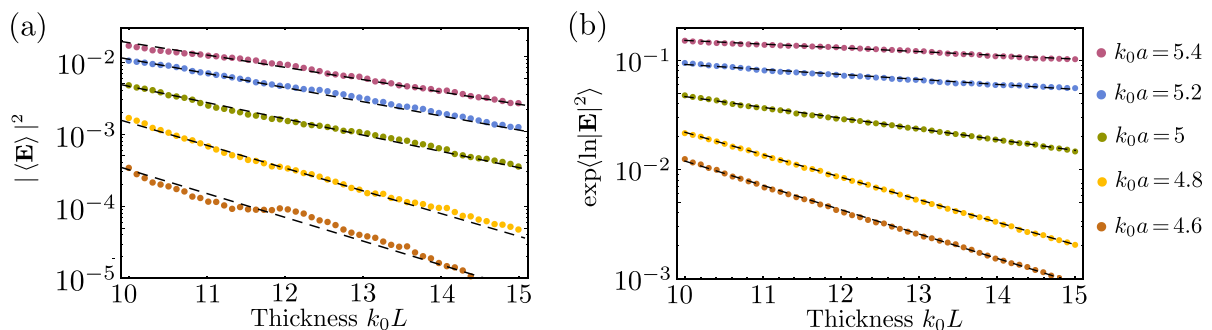

FIG. 16. Intensity of the average field (a) and average of the intensity logarithm (b) as function of the sample thickness L, evaluated for the geometry shown in Fig. 15 at $\delta = 0$. Dashed lines show the best linear fits.

function $G_0^t(r, \omega_0)$ with the far-field expansion of the average Green's function, $\langle G^t(r, \omega_0) \rangle \simeq G_0^t(r, \omega_0) e^{-r/2\ell_s}$.

We show in Fig. 14 the anisotropy factor g evaluated from Eq. (31) and Eq. (E2) with $U^\perp = U_C^\perp + U_B^\perp + U_L^\perp$, for the range of density probed in Fig. (12) and different values of detuning δ. In particular, at resonance ($\delta = 0$), we find $g \sim 0.07 - 0.13$, which gives $\ell_t \sim 1.07 - 1.15\, \ell_s$.

APPENDIX F: NUMERICAL EVALUATION OF ℓ_s AND ξ

The numerical estimate of the scattering mean free path ℓ_s and of the localization length ξ is performed through *ab initio* computations using the coupled dipoles method. We place a SHU pattern into a rectangle of length L (typically $kL \in [10, 60]$) and transverse size D. In order to mimic a slab geometry, which is the most convenient geometry to have access to estimates of ℓ_s and ξ, we choose $D \gg L$ (typically $D = 20L$, see Fig. 15). This system is shined using a gaussian beam of waist $w \gg \lambda$ (typically $kw = 200$) given by

$$\mathbf{E}(\mathbf{r}, \omega) = \frac{\mathbf{E}_0}{\sqrt{1 + i\alpha}} \exp\left[ikx - \frac{y^2}{w^2(1 + i\alpha)}\right] \quad \text{(F1)}$$

for TE waves. $\mathbf{E}_0$ is the amplitude and $\alpha = 2x/(kw^2)$. This specific illumination is chosen such that it smoothes the transverse finite-size effects. The transmitted electric field is computed for each disordered configuration on a screen of size d lying at a distance X from the output interface of the slab. We take $X > \lambda$ (typically $kX = 10$) in order to avoid potential near-field effects close to the interface.

In order to estimate ℓ_s, we average the transmitted field over many SHU configurations. To accelerate the numerical convergence, we also perform a spatial average over the observation screen assuming ergodicity and a size $d > \lambda$ (typically $kd = 10$). Then we compute the intensity of this average field and perform a fit with the formula

$$|\langle \mathbf{E} \rangle|^2 = A \exp\left[-\frac{L}{\ell_s}\right] \quad \text{(F2)}$$

as a function of the thickness of the slab L. A and ℓ_s are the fitted parameters. Results are presented in Fig. 16(a).

The estimate of the localization length ξ is performed from the fit of the average of the intensity logarithm as a function
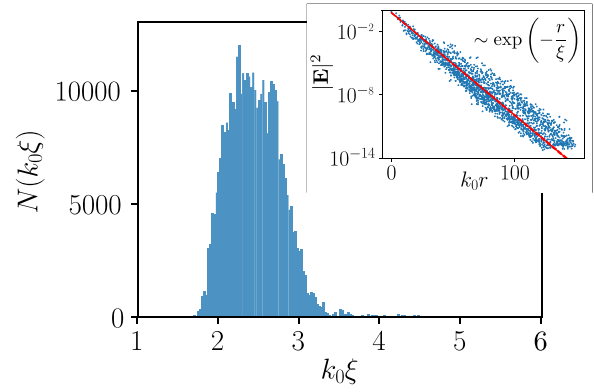

FIG. 17. Histogram of the localization length ξ obtained from a fit of the eigenstates of $\mathcal{H}(\omega_0)$ in the TE polarization, at $k_0 a = 4.5$ and $\chi = 0.5$. Here the eigenstates are associated to detuning $\delta \in [-0.05, 0.05]$. The inset shows an example of the intensity profile of an eigenstate with the best fitting estimate. A weighted fit with a $(1 + r)^{-1}$ penalty has been used to account for the variable number of data points with the distance r.

of L. The fitting formula is given by

$$\langle \ln |\mathbf{E}|^2 \rangle = B - L/\xi \quad \text{(F3)}$$

where B and ξ are the fitted parameters. Results are presented in Fig. 16(b). We also compared the value of ξ found from Eq. (F3) with the length characterizing the exponential profile of the eigenstates of $\mathcal{H}(\omega_0)$ (see inset of Fig. 17). The uncertainty on the fitting parameter for this length (also noted ξ in Fig. 17) is of the order of the percent, ensuring that the eigenstates are indeed exponentially localized. For a given value of $k_0 a$, eigenstates corresponding to a certain detuning δ do not necessarily have the same localization length ξ. However, in the regime of density and detuning where we expect strong localization, the distribution $p(\xi)$ becomes noticeably narrow. An example of $p(\xi)$ obtained in this way is shown in Fig. 17. The values of ξ represented in Fig. 12 correspond to the mean value of $p(\xi)$ and the error-bar to the standard deviation, computed for different $k_0 a$ at $\delta = 0$, using 32 SHU configurations of $N = 2000$ resonators distributed in a disk. For all $k_0 a$, the disk radius is significantly larger than ξ ($k_0 R \in [100 - 150]$).

[1] S. Yu, C.-W. Qiu, Y. Chong, S. Torquato, and N. Park, Engineered disorder in photonics, Nat. Rev. Mater. **6**, 226 (2021).

[2] K. Vynck, R. Pierrat, R. Carminati, L. S. Froufe Pérez, F. Scheffold, R. Sapienza, S. Vignolini, and J. J. Sáenz, Light in correlated disordered media, arXiv:2106.13892.

[3] G. B. Benedek, Theory of transparency of the eye, Appl. Opt. **10**, 459 (1971).

[4] G. Jacucci, S. Vignolini, and L. Schertel, The limitations of extending nature's color palette in correlated, disordered systems, Proc. Natl. Acad. Sci. USA **117**, 23345 (2020).

[5] L. F. Rojas-Ochoa, J. M. Mendez-Alcaraz, J. J. Sáenz, P. Schurtenberger, and F. Scheffold, Photonic Properties of Strongly Correlated Colloidal Liquids, Phys. Rev. Lett. **93**, 073903 (2004).

[6] S. Fraden and G. Maret, Multiple Light Scattering from Concentrated, Interacting Suspensions, Phys. Rev. Lett. **65**, 512 (1990).

[7] S. John, Strong Localization of Photons in Certain Disordered Dielectric Superlattices, Phys. Rev. Lett. **58**, 2486 (1987).

[8] P. D. García, R. Sapienza, C. Toninelli, C. López, and D. S. Wiersma, Photonic crystals with controlled disorder, Phys. Rev. A **84**, 023813 (2011).

[9] C. Jin, X. Meng, B. Cheng, Z. Li, and D. Zhang, Photonic gap in amorphous photonic materials, Phys. Rev. B **63**, 195107 (2001).

[10] K. Edagawa, S. Kanoko, and M. Notomi, Photonic Amorphous Diamond Structure with a 3D Photonic Band Gap, Phys. Rev. Lett. **100**, 013901 (2008).

[11] S. F. Liew, J.-K. Yang, H. Noh, C. F. Schreck, E. R. Dufresne, C. S. O'Hern, and H. Cao, Photonic band gaps in three-dimensional network structures with short-range order, Phys. Rev. A **84**, 063818 (2011).

[12] L. S. Froufe-Pérez, M. Engel, J. J. Sáenz, and F. Scheffold, Band gap formation and anderson localization in disordered photonic materials with structural correlations, Proc. Natl. Acad. Sci. USA **114**, 9570 (2017).

[13] M. Florescu, S. Torquato, and P. J. Steinhardt, Designer disordered materials with large, complete photonic band gaps, Proc. Natl. Acad. Sci. USA **106**, 20658 (2009).

[14] L. S. Froufe-Pérez, M. Engel, P. F. Damasceno, N. Muller, J. Haberko, S. C. Glotzer, and F. Scheffold, Role of Short-Range Order and Hyperuniformity in the Formation of Band Gaps in Disordered Photonic Materials, Phys. Rev. Lett. **117**, 053902 (2016).

[15] E. Lidorikis, M. M. Sigalas, E. N. Economou, and C. M. Soukoulis, Tight-Binding Parametrization for Photonic Band Gap Materials, Phys. Rev. Lett. **81**, 1405 (1998).

[16] K. Vynck, D. Felbacq, E. Centeno, A. I. Căbuz, D. Cassagne, and B. Guizal, All-Dielectric Rod-Type Metamaterials at Optical Frequencies, Phys. Rev. Lett. **102**, 133901 (2009).

[17] C. Rockstuhl, U. Peschel, and F. Lederer, A periodic structure mimics a metamaterial, Opt. Lett. **31**, 1741 (2006).

[18] S. R. Sellers, W. Man, S. Sahba, and M. Florescu, Local self-uniformity in photonic networks, Nat. Commun. **8**, 14439 (2017).

[19] A. Lagendijk and B. A. van Tiggelen, Resonant multiple scattering of light, Phys. Rep. **270**, 143 (1996).

[20] D. Weaire, Existence of a Gap in the Electronic Density of States of a Tetrahedrally Bonded Solid of Arbitrary Structure, Phys. Rev. Lett. **26**, 1541 (1971).

[21] M. F. Thorpe and D. Weaire, Electronic Density of States of Amorphous Si and Ge, Phys. Rev. Lett. **27**, 1581 (1971).

[22] S. Imagawa, K. Edagawa, K. Morita, T. Niino, Y. Kagawa, and M. Notomi, Photonic band-gap formation, light diffusion, and localization in photonic amorphous diamond structures, Phys. Rev. B **82**, 115116 (2010).

[23] M. Rechtsman, A. Szameit, F. Dreisow, M. Heinrich, R. Keil, S. Nolte, and M. Segev, Amorphous Photonic Lattices: Band Gaps, Effective Mass, and Suppressed Transport, Phys. Rev. Lett. **106**, 193904 (2011).

[24] G. M. Conley, M. Burresi, F. Pratesi, K. Vynck, and D. S. Wiersma, Light Transport and Localization in Two-Dimensional Correlated Disorder, Phys. Rev. Lett. **112**, 143901 (2014).

[25] J. Haberko, L. S. Froufe-Pérez, and F. Scheffold, Transition from light diffusion to localization in three-dimensional amorphous dielectric networks near the band edge, Nat. Commun. **11**, 4867 (2020).

[26] G. J. Aubry, L. S. Froufe-Pérez, U. Kuhl, O. Legrand, F. Scheffold, and F. Mortessagne, Experimental Tuning of Transport Regimes in Hyperuniform Disordered Photonic Materials, Phys. Rev. Lett. **125**, 127402 (2020).

[27] P. Sheng, *Introduction to Wave Scattering, Localization and Mesoscopic Phenomena* (Springer-Verlag, Berlin, 2006).

[28] H. Hu, A. Strybulevych, J. H. Page, S. E. Skipetrov, and B. A. van Tiggelen, Localization of ultrasound in a three-dimensional elastic network, Nat. Phys. **4**, 945 (2008).

[29] S. John, Localization of light, Phys. Today **44**(5), 32 (1991).

[30] S. John, Localization of light: Theory of photonic band gap materials, in *Photonic Band Gap Materials*, edited by C. M. Soukoulis (Springer Netherlands, Dordrecht, 1996), pp. 563–665.

[31] E. Abrahams, P. W. Anderson, D. C. Licciardello, and T. V. Ramakrishnan, Scaling Theory of Localization: Absence of Quantum Diffusion in Two Dimensions, Phys. Rev. Lett. **42**, 673 (1979).

[32] D. Vollhardt and P. Wölfle, Self-consistent theory of anderson localization, in *Electronic Phase Transitions*, edited by W. Hanke and Y. V. Kopaev (Elsevier Science Publishers, Amsterdam, 1992), pp. 1–78.

[33] M. Antezza and Y. Castin, Spectrum of Light in a Quantum Fluctuating Periodic Structure, Phys. Rev. Lett. **103**, 123903 (2009).

[34] J. Perczel, J. Borregaard, D. E. Chang, H. Pichler, S. F. Yelin, P. Zoller, and M. D. Lukin, Photonic band structure of two-dimensional atomic lattices, Phys. Rev. A **96**, 063801 (2017).

[35] S. E. Skipetrov, Finite-size scaling of the density of states inside band gaps of ideal and disordered photonic crystals, Eur. Phys. J. B **93**, 70 (2020).

[36] A. Goetschy and S. E. Skipetrov, Non-Hermitian Euclidean random matrix theory, Phys. Rev. E **84**, 011150 (2011).

[37] S. E. Skipetrov and I. M. Sokolov, Absence of Anderson Localization of Light in a Random Ensemble of Point Scatterers, Phys. Rev. Lett. **112**, 023905 (2014).

[38] L. Bellando, A. Gero, E. Akkermans, and R. Kaiser, Cooperative effects and disorder: A scaling analysis of the spectrum of the effective atomic hamiltonian, Phys. Rev. A **90**, 063822 (2014).

[39] C. E. Máximo, N. Piovella, P. W. Courteille, R. Kaiser, and R. Bachelard, Spatial and temporal localization of light in two dimensions, Phys. Rev. A **92**, 062702 (2015).

[40] S. E. Skipetrov, Finite-size scaling analysis of localization transition for scalar waves in a three-dimensional ensemble of resonant point scatterers, Phys. Rev. B **94**, 064202 (2016).

[41] T. M. Nieuwenhuizen, A. Burin, Y. Kagan, and G. Schlyapnikov, Light propagation in a solid with resonant atoms at random positions, Phys. Lett. A **184**, 360 (1994).

[42] S. E. Skipetrov and J. H. Page, Red light for anderson localization, New J. Phys. **18**, 021001 (2016).

[43] B. A. van Tiggelen and S. E. Skipetrov, Longitudinal modes in diffusion and localization of light, Phys. Rev. B **103**, 174204 (2021).

[44] L. L. Foldy, The multiple scattering of waves. I. General theory of isotropic scattering by randomly distributed scatterers, Phys. Rev. **67**, 107 (1945).

[45] M. Lax, Multiple scattering of waves, Rev. Mod. Phys. **23**, 287 (1951).

[46] R. H. Lehmberg, Radiation from an *n*-atom system. I. General formalism, Phys. Rev. A **2**, 883 (1970).

[47] A. Goetschy, Light in disordered atomic systems: Euclidean matrix theory of random lasing. Ph.D. thesis, J. Fourier University–Grenoble 1, France, 2011, https://tel.archives-ouvertes.fr/tel-00676988v1.

[48] J. A. Klugkist, M. Mostovoy, and J. Knoester, Mode Softening, Ferroelectric Transition, and Tunable Photonic Band Structures

in a Point-Dipole Crystal, Phys. Rev. Lett. **96**, 163903 (2006).

[49] M. Antezza and Y. Castin, Fano-Hopfield model and photonic band gaps for an arbitrary atomic lattice, Phys. Rev. A **80**, 013816 (2009).

[50] E. Akkermans, A. Gero, and R. Kaiser, Photon Localization and Dicke Superradiance in Atomic Gases, Phys. Rev. Lett. **101**, 103602 (2008).

[51] S. E. Skipetrov and A. Goetschy, Euclidean random matrices for waves in random media, J. Phys. A: Math. Theor. **44**, 065102 (2011).

[52] A. Goetschy and S. E. Skipetrov, Euclidean matrix theory of random lasing in a cloud of cold atoms, Europhys. Lett. **96**, 34005 (2011).

[53] S. Torquato, Hyperuniform states of matter, Phys. Rep. **745**, 1 (2018).

[54] S. Torquato, G. Zhang, and F. H. Stillinger, Ensemble Theory for Stealthy Hyperuniform Disordered Ground States, Phys. Rev. X **5**, 021020 (2015).

[55] O. Leseur, R. Pierrat, and R. Carminati, High-density hyperuniform materials can be transparent, Optica **3**, 763 (2016).

[56] S. E. Skipetrov and I. M. Sokolov, Ioffe-Regel criterion for anderson localization in the model of resonant point scatterers, Phys. Rev. B **98**, 064207 (2018).

[57] R. Monsarrat, Propagation of light waves in correlated disordered media: density of states, transport, localisation, Ph.D. thesis, PSL University, 2022, https://tel.archives-ouvertes.fr/tel-03765743.

[58] S. E. Skipetrov, Localization of light in a three-dimensional disordered crystal of atoms, Phys. Rev. B **102**, 134206 (2020).

[59] J.-K. Yang, C. Schreck, H. Noh, S.-F. Liew, M. I. Guy, C. S. O'Hern, and H. Cao, Photonic-band-gap effects in two-dimensional polycrystalline and amorphous structures, Phys. Rev. A **82**, 053838 (2010).

[60] A. Goetschy and S. Skipetrov, Euclidean random matrices and their applications in physics, arXiv:1303.2880.

[61] E. Akkermans and G. Montambeaux, *Mesoscopic Physics of Electrons and Photons* (Cambridge University Press, Cambridge, 2007).

[62] B. A. van Tiggelen and A. Lagendijk, Resonantly induced dipole-dipole interactions in the diffusion of scalar waves, Phys. Rev. B **50**, 16729 (1994).

[63] O. Morice, Y. Castin, and J. Dalibard, Refractive index of a dilute Bose gas, Phys. Rev. A **51**, 3896 (1995).

[64] N. Cherroret, D. Delande, and B. A. van Tiggelen, Induced dipole-dipole interactions in light diffusion from point dipoles, Phys. Rev. A **94**, 012702 (2016).

[65] D. E. Chang, J. S. Douglas, A. González-Tudela, C.-L. Hung, and H. J. Kimble, Colloquium: Quantum matter built from nanoscopic lattices of atoms and photons, Rev. Mod. Phys. **90**, 031002 (2018).

[66] O. U. Uche, F. H. Stillinger, and S. Torquato, Constraints on collective density variables: Two dimensions, Phys. Rev. E **70**, 046122 (2004).

[67] O. U. Uche, S. Torquato, and F. H. Stillinger, Collective coordinate control of density distributions, Phys. Rev. E **74**, 031104 (2006).

[68] R. D. Batten, F. H. Stillinger, and S. Torquato, Classical disordered ground states: Super-ideal gases and stealth and equi-luminous materials, J. Appl. Phys. **104**, 033504 (2008).

[69] C. C. Kwong, D. Wilkowski, D. Delande, and R. Pierrat, Coherent light propagation through cold atomic clouds beyond the independent scattering approximation, Phys. Rev. A **99**, 043806 (2019).